NIR Imagery based Grass Fire Detection and Metrics Measurement using Small UAS

Jacksen Goyer

Submitted to the graduate degree program in Department of Aerospace Engineering and the Graduate Faculty of the University of Kansas in partial fulfillment of the requirements for the degree of Master of Science.

Dr. Haiyang Chao, Chairperson

Committee members

Dr. Ray Taghavi

Dr. Craig McLaughlin

Date defended: August 04, 2022

The Thesis Committee for Jacksen Goyer certifies
that this is the approved version of the following thesis :

NIR Imagery based Grass Fire Detection and Metrics Measurement using Small UAS

Dr. Haiyang Chao, Chairperson

Date approved: September 06, 2022

Abstract

This thesis focuses on the generation of a new grass fire aerial image dataset and development of novel methods for near-infrared (NIR) imagery-based fire front identification and fire depth estimation using small unmanned aircraft systems (sUAS). The procedure for collection and creation of the Grass Fire Front and near-Infrared (NIR) and Thermal Imagery (GRAFFITI) dataset is introduced first including two levels of data: synced raw thermal and red, green and near-infrared (RGNIR) image pairs and processed image pairs of the same overlapping field-of-view. A novel NIR imagery-based fire detection and fire front identification algorithm is then proposed and validated against manually labeled ground truth, using the GRAFFITI dataset. A comparative study is further performed on the problem of grass fire front location and flame depth estimation using thermal and NIR imagery. Finally, recommendations are made to future researchers who are interested in wildland fire sensing using thermal or NIR imagery.

Acknowledgements

First and foremost, I would like to thank my parents, Michele and Dennis, and my grandparents, Jackie and Christina for their continual love and support. Thank you for believing in my academic and professional interests and all the sacrifices you made to help me gain the confidence to succeed at whatever I set my mind to. I would also like to thank my significant other, Jordan. I am forever thankful for you helping me get through grad school, and of course that smile of yours.

I would like to send my highest thanks to my advisor, Dr. Haiyang Chao. I have worked under you for over five years now and have enjoyed every minute. Your instruction and guidance have led me to become not only a better engineer, but a better person with a wider interest in how our work on aircraft can provide a brighter future.

An additional thank you goes to my other committee members, Dr. Ray Taghavi and Craig McLaughlin. Thank you all for being patient with me throughout this process.

Included in my thanks are all the professors and staff in the aerospace department that have helped me throughout my time at KU. I've had many questions and requested the time and effort of most of the department and I appreciate every second that you all provided. Additional thanks to all the friends I met during my time in Lawrence. Without everyone at KU, I would quite literally not be here.

Final thanks go to my colleagues at the CUSL: Dr. Pengzhi Tian, Dr. Saket Gowravaram, Dr. Harold Flanagan, Justin Matt, Zhenghao Lin, Mosarruf Hossain, Connor Kinkade, Luke Hersh, and Adam Baruth. Between the flight tests and time

spent in the lab, you all have helped me become an overall better human and I will forever appreciate it.

I would like to acknowledge the following grants for funding this research: University of Kansas Research GO Grant, US Department of Agriculture (USDA) National Institute of Food and Agriculture (NIFA) Grant 2019-67021-28992, and Kansas Water Resources Institute USGS 104(b) Water Resources Research Grant 2018KS198B.

Contents

List of Figures

List of Tables

Chapter 1

Introduction

1.1 Motivation and Background

Wildfire detection, monitoring, and prediction are critical to fire fighting operations that attempt to mitigate and prevent damage to forests, residential areas, sensitive wildlife habitats and other ecosystems. Traditional remote sensing solutions for wildfire detection and monitoring can be grouped into ground-based, aircraft-based and satellite-based systems [3, 4]. Ground-based systems can measure high resolution flame characteristics in the camera field of view, but has a limited range. Satellites can provide quick detection of wildfires using a wide range of spectra, but image fires at a low spatial and temporal resolution. Manned aircraft provide a middle point between satellites and ground-based systems but are expensive and can put a pilot's life in danger due to the hazardous conditions present. Small unmanned aerial systems (sUAS) have recently gained interests as a low-cost solution for wildfire monitoring and detection. With minimal human intervention, wide and adjustable viewpoints, and fast deployment, sUAS can offer an accessible platform for superfine spatial and temporal resolution mapping of wildfires.

One of the most important steps for sUAS-based wildfire sensing is fire pixel identification within the image frame. Challenges for aerial fire identification include smoke occlusion, differing fire conditions, changing environmental colors and illuminations, etc. Thermal cameras are widely used for fire detection since heat radiation can be measured through smoke or at night; however, thermal solutions are very expensive. This motivates the use of low-cost cameras that image visible and non-visible spectral bands, such as near-infrared (NIR) cameras which improve upon the contrast between fire and the background environment [5]. Although ground-based NIR imagery

has been used for fire pixel detection and comparison with RGB cameras, few have performed UAS-based fire detection [2].

Another critical factor for validation of fire spread models and analysis on wildfire metrics measurement is the creation of benchmark datasets of wildland fires. Ground cameras have been used to generate datasets comparing the representation of fires in different spectral bands, however the ground-view perspective obfuscates other sections of the fire [5, 6]. Aerial images can provide a top view of fire evolution, but existing wildfire aerial datasets do not provide the same view of the fire in different spectra. To ensure accurate fire metric measurement and real-time fire front detection, multispectral datasets with the same field of view of the fire need to be created and analyzed for future wildfire fighting.

1.2 Contributions

This thesis focuses on the creation of a new fire imagery dataset taken from a fixed-wing sUAS flying at low altitudes and development of novel fire metrics measurement algorithms. The primary contributions of this thesis can be summarized as follows:

1. Developed a procedure to rectify, align, and register uncalibrated NIR and thermal images from an sUAS over a wildland grass fire;

2. Generated the GRAFFITI dataset: a new sUAS fire dataset which includes both airborne NIR and thermal imagery sharing the same field of view during a grassland fire;

3. Proposed a novel NIR imagery-based fire identification and fire front detection algorithm for grass fires;

4. Performed a comparative study between NIR and thermal aerial images for grass fire front detection and flame depth estimation.

1.3 Thesis Organization

The thesis is organized as the following: the thesis motivation, background and contributions were discussed in Chapter 1. Chapter 2 details the creation and initial analysis of the GRAFFITI dataset. A rule-based fire detection and fire front identification algorithm using the NIR imagery is presented in Chapter 3. Chapter 4 discusses the difference between the thermal and RGNIR images for estimation of grass fire front location and flame depth. Finally, future work and conclusion are summarized in Chapter 5.

Chapter 2

GRAFFITI: GRAss Fire Front near-Infrared and Thermal Imagery Dataset

2.1 Chapter Introduction

This chapter focuses on the creation of the GRAss Fire Front near-Infrared and Thermal Imagery (GRAFFITI) dataset, which consists of red, green and near-infrared (RGNIR) imagery paired with thermal IR images over grass fire fronts collected by a small UAS (sUAS). The objective for creating this dataset is to support flame and wildland fire characteristic analysis. Researchers have used different imaging techniques to determine fire behavior metrics like rate of spread (ROS), residence time, and spread direction [7]. While satellite and manned aircraft have been frequently used in the past to gather wildfire and grass fire data, sUAS have recently emerged as a low-cost and safe wildfire sensing platform due to the spatial and temporal resolution improvements. Additionally, the nadir view directly above fires from sUAS reduces challenges from registration and geometric correction of fire imagery, compared with ground-based solutions [8].

Besides the sensing platforms, the spectral band of the camera is also a critical factor for the observations of fire. Thermal infrared (TIR or IR) cameras are widely used for visualizing fire as the high radiation output from wildfires are highly sensitive in the TIR spectrum [7, 9, 10]. However, most thermal cameras are expensive (>$4,000) and have a relatively low spatial resolution when compared to a traditional visual spectrum camera, which offers high pixel resolution but suffers from smoke occlusion. Near infrared (NIR) is another spectral band with improved radiance observation of fire compared with RGB cameras. Commonly used in vegetation observation [11], NIR

imagery improves the visual spectrum observation of fire by having reduced smoke occlusion and an increased visual contrast between active flaming regions and the background environment [5].

Former researchers have generated fire datasets and mostly focused on fire detection using a single spectrum or spectrum comparisons on fire identification. The FLAME dataset [12] was collected using quadcopters over prescribed slash pile burns in the thermal and RGB spectrums. However, the dataset was more suited for fire segmentation and detection, not for fire metric analysis given the oblique perspective and missing spatiotemporal information. Additionally, the thermal and RGB images were taken during different flights or at different times during flight over different sections of the controlled burn. Burnett [5] offers a comparison of RGB and NIR detection of burn piles from a ground perspective. While verifying that fire pixels are easier to identify in the NIR imagery and are less sensitive to smoke occlusion compared with RGB images, the perspective of this dataset does not allow for georeferencing or fire metrics derivation. The Corsian Fire dataset [6] has over 500 images of RGB and NIR images of fire with a ground truth mask, but also only provides a ground perspective.

Most existing grass fire or wildfire image sets are taken at a low pixel resolution or used primarily for fire detection. The GRAFFITI dataset offers 20 pairs of IR and RGNIR nadir imagery that observes the same sections of a grass fire during the fire evolution. Additionally, the collected image pairs are manually registered with respect to each other for the same fire scene observation at different spectral bands.

This chapter is organized as the following. Section 2.2 provides an overview of the KHawk-55T sUAS and the prescribed fire experiment. Section 2.3 focuses on the procedure to generate the GRAFFITI dataset, including synchronization, distortion rectification, manual registration, and preliminary analysis on the homography estimation accuracy.

2.2 KHawk-55T sUAS & Grass Fire Experiment

2.2.1 KHawk-55T sUAS

The KHawk-55T aircraft was used for the raw GRAFFITI data collection, which was created by Cooperative Unmanned Systems Lab (CUSL) researchers for remote sensing and cooperative control missions. The KHawk-55T sUAS is a ZII Wing model shown in Fig. 2.1 [13]. It has a wingspan of 55 inches and a 20-30 minute endurance. The KHawk-55T sUAS can support manual and autonomous flights through the onboard Pixhawk Cube autopilot and a Ublox Neo-M8N GPS which has a horizontal position accuracy of 2.5 m circular error probable (CEP) [14].

Figure 2.1: KHawk-55T fixed-wing sUAS.

The KHawk-55T is also equipped with two cameras for multispectral remote sensing: the FLIR Vue Pro R and the PeauPro82 NDVI GoPro, shown in Fig. 2.2. The camera specifications are provided in Table 2.1. Both cameras are light-weight and were specifically chosen for remote sensing of wildland fires as the red, green, NIR and thermal bands collected by the cameras can assist in capturing the difference in burned and unburned areas, the presence of smoke, and ground temperature gradients. Both cameras were secured in the KHawk-55T using foam blocks. While ensuring the viewpoint of the cameras were unobstructed during flight, this mounting method allowed for small movements of both cameras which generated challenges for later image registration.

The FLIR Vue Pro R thermal camera is specifically designed for sUAS-based temperature measurements, with the ability to generate geo-tagged images through communication with the Pixhawk autopilot. The Vue Pro R has two range settings for capturing temperature data using

Table 2.1: KHawk-55T camera specifications.

Specification	PeauPro82 Modified NDVI [1]	FLIR Vue Pro R [15]
Weight	90 g	142 g
Spectral Response	630-900 nm	7.5-13.5 μm
Update Rate	29.97 Hz	up to 30 Hz
Resolution	1920 $\times$ 1080 pix	640 $\times$ 512 pix
Field of View	74° $\times$ 45°	69° $\times$ 56°

Figure 2.2: FLIR Vue Pro R (left) and PeauPro82 NDVI GoPro Hero 4 Black (right).

14-bit TIFF images: low-gain (-25/+550 °C) with a pixel sensitivity of 0.04 °C and high-gain (-25/+135 °C) with a pixel sensitivity of 0.4 °C [16].

The PeauPro82 is a modified GoPro Hero 4 that replaces the blue channel of the visible spectrum sensor with an NIR band, which has been used for plant growth quantification [17]. In this thesis, data from the inexpensive GoPro camera is used mainly for the NIR channel (Fig. 2.3). Compared to the response of fire in the visible spectrum, flame signatures in the NIR spectrum are stronger and more reliable for fire detection and monitoring [8]. Additionally, a combination of the NIR and visual bands can help determine the fire front and depth more accurately than a single spectral band.

2.2.2 Prescribed Grass Fire Experiment & Raw Aerial Imagery

On October 8th, 2019, a prescribed fire was performed between 11:38 AM and 12:25 PM CDT at the Anderson County Prairie Preserve, which is managed by the Kansas Biological Survey (KBS). The controlled burn consisted primarily of tallgrasses within the approximately 530 m $\times$ 250 m rectangular area. A side view of the fire is shown in Fig. 2.4, taken by a DJI quadcopter. Two

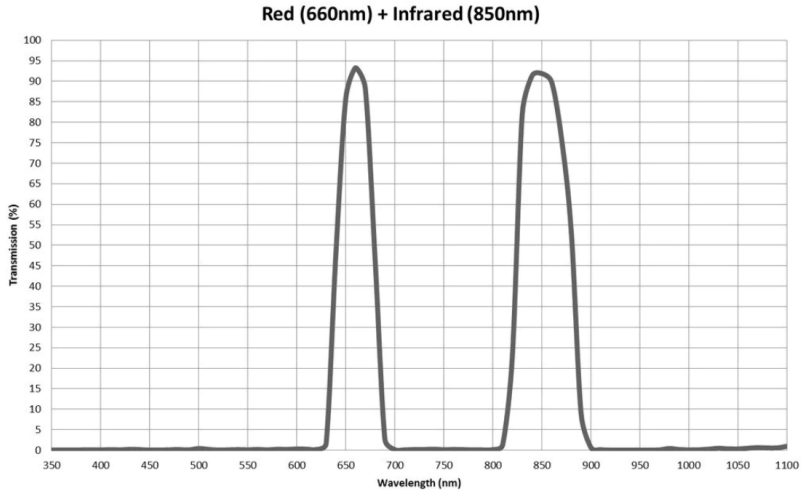

Figure 2.3: PeauPro82 NDVI camera spectral response [1].

teams from KBS set up the prescribed fire by starting at the midpoint of the Northern boundary and moved in opposite directions. The average wind velocity during the burn was 6.26 $\frac{m}{s}$ from the south based on measurements from a Campbell Scientific CSAT3B wind anemometer installed about 1.9 m above the ground [2]. From 12:06:05 PM to 12:17:47 PM, the KHawk-55T sUAS with the thermal and RGNIR imaging payload flied over the controlled burn at an altitude of about 120 m above ground level.

Images from different flyovers of the same corner of the fire front from the onboard cameras are shown in Fig. 2.5. The histogram of the thermal images shown in this paper have been adjusted for an improved view of the background. Raw thermal images are dark except for high temperature areas like fire. For visualizing overlapped features to support later stitching and rectification, the thermal images were taken in the high-gain setting. This allowed for the surrounding environment to be clearer in thermal images after histogram adjustments; the low-gain setting would provide a finer resolution of the fire temperature, but the objects around the fire would be difficult to determine for further analysis such as generating orthomosaic maps [2] or the feature identification used later in this chapter.

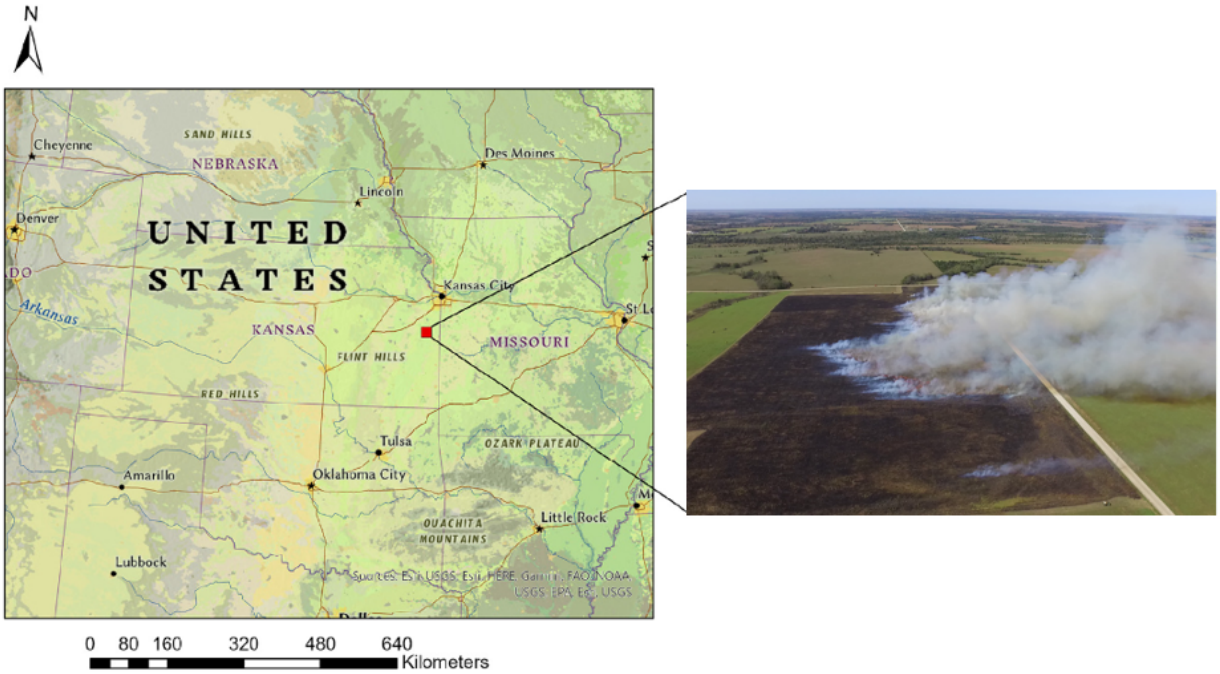

Figure 2.4: Anderson County fire field [2].

2.3 GRAFFITI Dataset

This section provides details on the process of acquiring, syncing, and distortion removal necessary to create a dataset that observes a controlled burn from the thermal and RGNIR spectrums. The GRAFFITI dataset includes two levels of data. The level 1 dataset consists of 20 RGNIR and thermal image pairs that are synchronized after both spectral images are tagged with a GPS position and corresponding camera orientation. The GRAFFITI level 2 dataset includes 15 processed RGNIR and thermal image overlays, which share the same field of view. The process of generating the GRAFFITI dataset is shown in Fig. 2.6. Beginning with raw thermal images (1 Hz), RGNIR video (29.97 Hz) and Pixhawk telemetry (5 Hz GPS and 25 Hz attitude), the RGNIR images are geo-tagged and the thermal image distortion is rectified. After pairing all thermal images with corresponding RGNIR frames, the pairs are down selected to create the GRAFFITI level 1 dataset. After manual feature matching, the homography between the selected 15 image pairs is estimated and used to create the GRAFFITI level 2 dataset of thermal and RGNIR overlays. Analysis is performed on the accuracy of feature matching and the overlap produced when transforming the

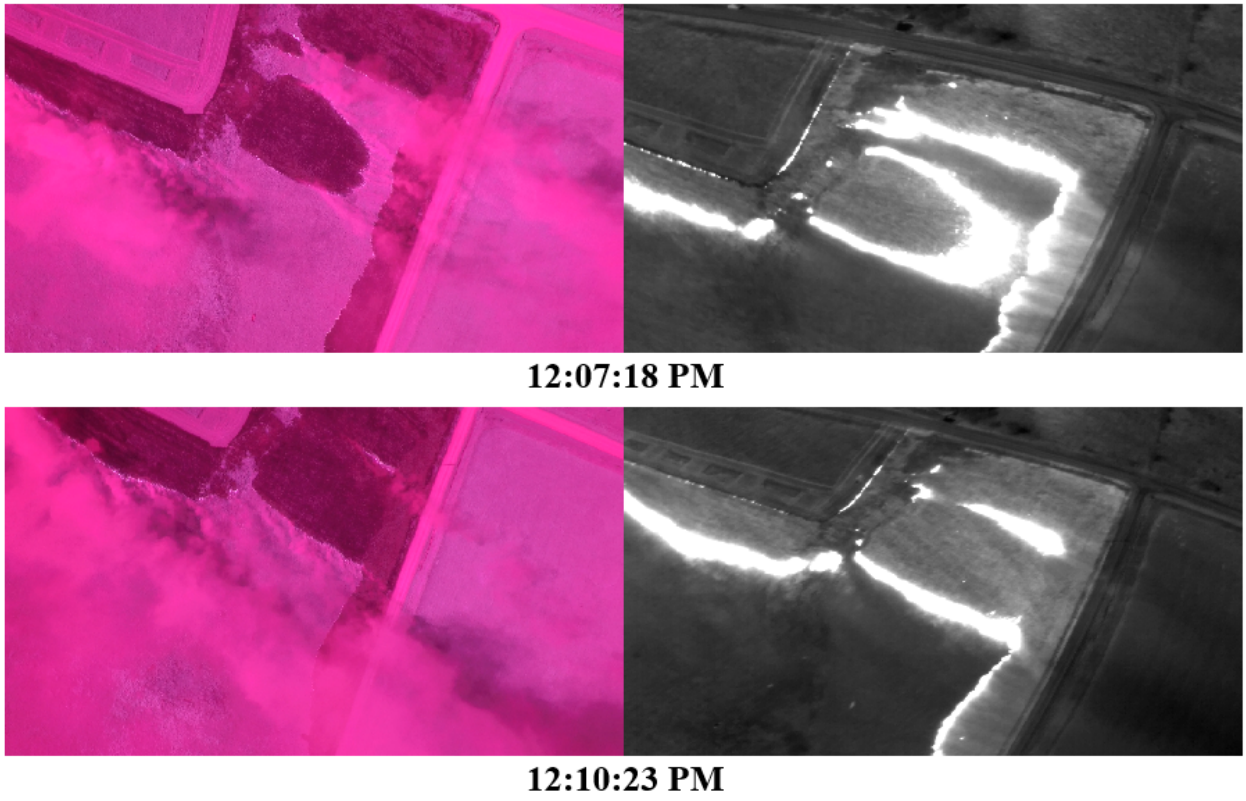

Figure 2.5: Example KHawk-55T image pairs of the same area from two different times in RGNIR (left) and histogram-adjusted thermal (right) bands.

RGNIR images into the thermal image space.

2.3.1 GRAFFITI Image Pair Synchronization

The fire data acquisition from both RGNIR and thermal bands present the opportunity for a unique dataset where multiple spectral bands can be observed and analyzed at a relatively high resolution for fire front observation applications. For a fair comparison between different spectral bands, it is desirable that the PeauPro82 and the FLIR Vue Pro R share the same nadir view of the fire. However, while the FLIR Vue Pro R has automatic geotagging built into the camera that can provide the geolocation information of the camera, the PeauPro82 does not have the same capability. Manual synchronization can be used instead to align each RGNIR image with the corresponding GPS and camera orientation information from the Pixhawk datalog. As the RGNIR video has a high frame rate of 29.97 Hz, along with 25 Hz orientation estimates and a 4 Hz GPS, the time of

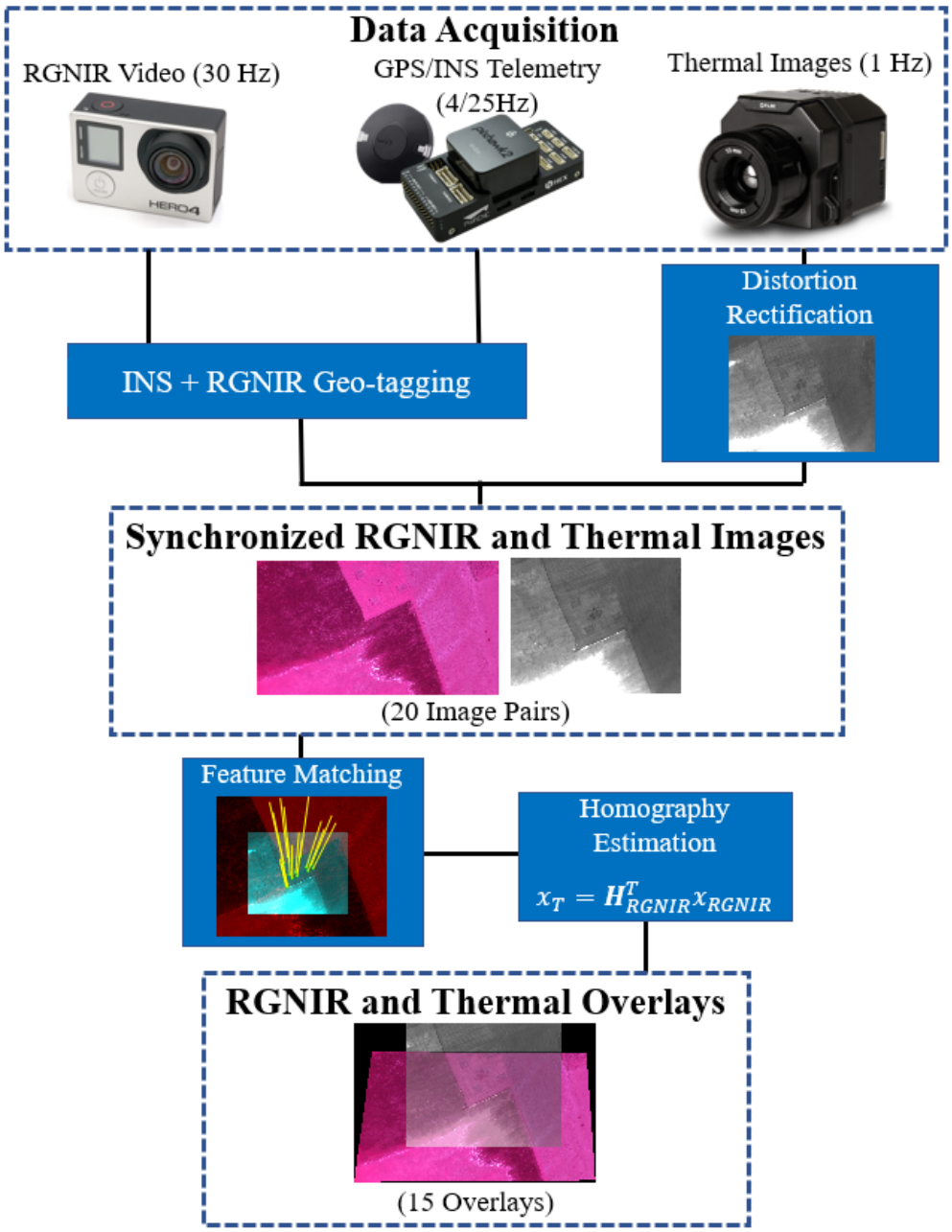

Figure 2.6: Flow diagram for generating the GRAFFITI dataset.

takeoff can be easily determined based on acceleration measurements during the bungee takeoff. In the ideal case, each pair of RGNIR and thermal images would be aligned for comparison after the synchronization process. However, as discussed in the next two sections, further fine tuning is sometimes needed to find the matched RGNIR and thermal image pairs both for synchronization and overlap comparisons before a full comparison can be performed.

2.3.2 Distortion Removal for Thermal Imagery

As shown in the left image of Fig. 2.7, the raw thermal image from the FLIR Vue Pro R has nontrivial distortions that present the straight edges of the road and sides of the fire area as having slight curvature. Before comparing the thermal images to the respective RGNIR image pairs, the distortion present in the Vue Pro R needs to be rectified (Fig. 2.7).

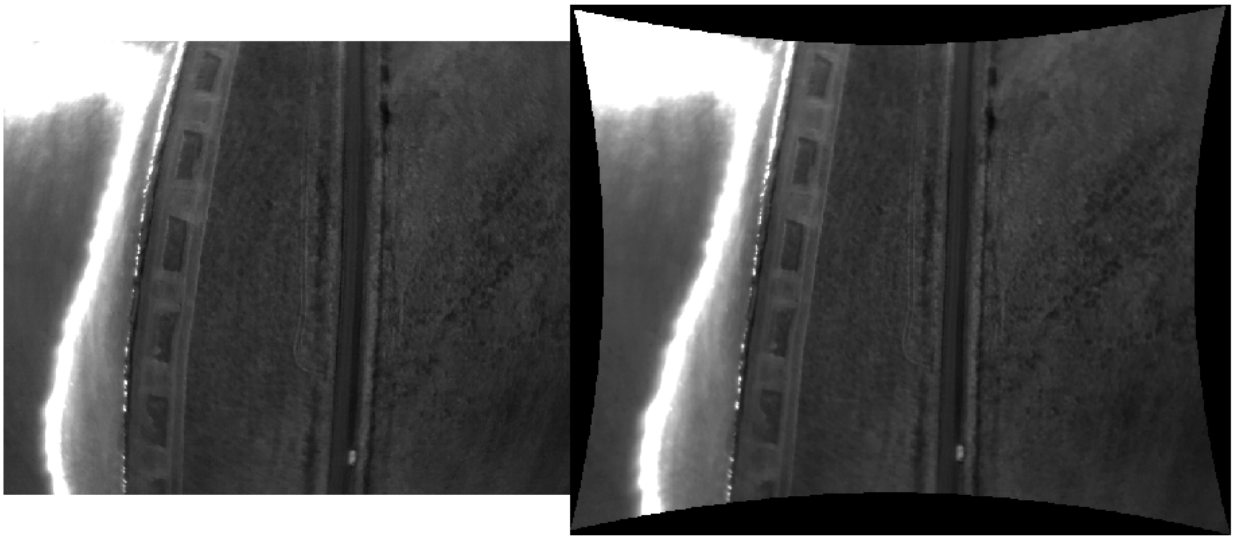

Figure 2.7: Raw (left) and zero-padded undistorted (right) thermal images.

The primary distortion models used on the thermal images were radial and tangential distortion, which are the lens distortion phenomenon when representing a real camera from a simplified ideal pinhole camera model. Radial distortion, also known as pincushion or barrel distortion, bends light near the edges of the lens at a greater angle than at the optical center of a camera. Equations 2.1 and 2.2 present the definitions of radial distortion where $x_{r,distorted}$ and $y_{r,distorted}$ are the radially distorted point locations, x and y are the undistorted pixel locations, k_1, k_2, and k_3 are radial distortion coefficients of the lens and r is the Euclidean distance from the image coordinate center ($r^2 = x^2 + y^2$).

$$x_{r,distorted} = x(1 + k_1 r^2 + k_2 r^4 + k_3 r^6) \tag{2.1}$$

$$y_{r,distorted} = y(1 + k_1 r^2 + k_2 r^4 + k_3 r^6) \tag{2.2}$$

Tangential distortion occurs when the lens of a camera and the image sensor are not parallel, the relative distance between objects at difference edges of the frame can be perceived larger than in reality. The equations describing the relation between the tangentially distorted pixel locations ($x_{t,distorted}$, $y_{t,distorted}$) and the undistorted pixel locations (x, y) are shown below where p_1 and p_2 are tangential distortion coefficients of the lens.

$$x_{t,distorted} = x + [2p_1xy + p_2(r^2 + 2x^2)] \tag{2.3}$$

$$y_{t,distorted} = y + [p_1(r^2 + 2y^2) + 2p_2xy] \tag{2.4}$$

Agisoft Photoscan software was used to generate thermal orthomosaic map using thermal images from the same flight used in this thesis, as discussed in [2]. Through the process of stitching and generating a fire map, the Agisoft software also produced an estimation for the intrinsic characteristics of the FLIR Vue Pro R used in the KHawk-55T, including the radial and tangential coefficients described above. The values used to remove distortion from the thermal images in the GRAFFITI dataset (Table 2.2) were generated by Agisoft Photoscan using an orthomosaic that produced a total error of 4.44 m over a total of 118 aerial images.

Table 2.2: KHawk-55T camera distortion coefficients.

Camera	k_1	k_2	k_3	p_1	p_2
FLIR Vue Pro R	-0.379	0.226	-0.084	-0.0004	0.0005
PeauPro82 GoPro	0.085	-0.098	0.020	-0.0001	-0.0001

An example image pair before and after the distortion removal is shown in Fig. 2.7. It can be observed that the gravel road appeared to be curved in the raw thermal image but not in the rectified image. For use in the GRAFFITI dataset, the portions of the image that include the zero-padding are removed, creating a 640 $\times$ 512 pixel image that represents the undistorted thermal image. The PeauPro82 has negligible lens distortion (Table 2.2) when using the same estimation method as the Vue Pro R, therefore the raw RGNIR images were directly used for registration.

2.3.3 NIR to FLIR Manual Image Registration

With rectified thermal images, initial comparison between the synced RGNIR and thermal images were performed. Due to the GPS error, the initial synced image pairs may be off by an offset, which is time variant probably caused by the small movements of the cameras. By observing attitude changes in the NIR and thermal image sequence as well as comparing the similarities of the fire coverage, the image pairs were manually adjusted to provide an NIR image that closely resembled the thermal image than the initial NIR sync. Fig. 2.8 presents an example image pair from the GRAFFITI dataset.

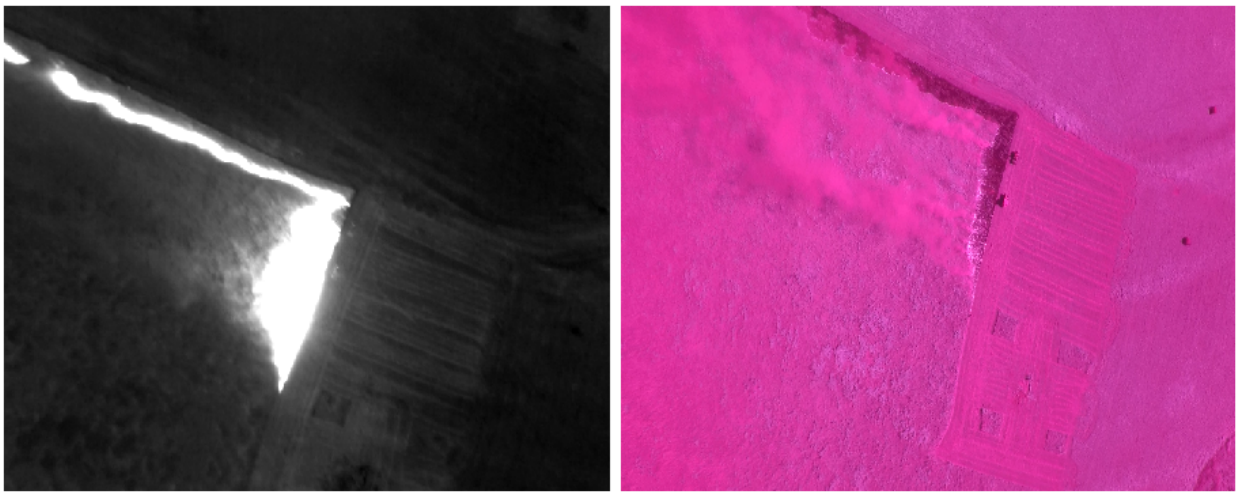

Figure 2.8: Example synchronized thermal (a) and RGNIR (b) image pair (12:10:35 PM).

After the manual final synchronization process, all thermal images from the Anderson County prescribed fire flight have a matching RGNIR image. The purpose of the GRAFFITI dataset is to find the synced thermal and RGNIR observation of the grass fire front to support fire metrics measurement analysis. Therefore, finding a match between an RGNIR pixel and a thermal pixel is required for observation and comparison. Using the pinhole camera model to represent the thermal (T) and RGNIR (NIR) images, a point in the world coordinate system (X,Y,Z) with the aircraft center of gravity as the origin, seen in both the thermal and RGNIR image coordinate systems are shown in Equations 2.5 and 2.6, respectively. The intrinsic matrix ($\mathbf{K}$) for both equations represent

the internal characteristics of the cameras: the focal lengths (f_x, f_y) and optical center (c_x, c_y) in pixels. Table 2.3 presents the intrinsic values for the PeauPro82 and the FLIR Vue Pro R.

$$\begin{bmatrix} \mu_T \\ \nu_T \\ 1 \end{bmatrix} = \frac{1}{Z} \begin{bmatrix} f_x & 0 & c_x \\ 0 & f_y & c_y \\ 0 & 0 & 1 \end{bmatrix} \begin{bmatrix} X \\ Y \\ Z \end{bmatrix} = \frac{1}{Z} \mathbf{K}_T \begin{bmatrix} X \\ Y \\ Z \end{bmatrix} \tag{2.5}$$

$$\begin{bmatrix} \mu_{NIR} \\ \nu_{NIR} \\ 1 \end{bmatrix} = \frac{1}{Z} \mathbf{K}_{NIR} \begin{bmatrix} X \\ Y \\ Z \end{bmatrix} \tag{2.6}$$

Table 2.3: KHawk-55T camera intrinsics.

Camera	Focal Length (f_x, f_y) [pix]	Optical Center (c_x, c_y) [pix]
PeauPro82 GoPro	(1197.17, 1197.17)	(7.55, 15.89)
FLIR Vue Pro R	(555.57, 555,57)	(-7.54, -4.37)

Since the same points show up in both the RGNIR and thermal images, both equations above can be used to describe a transformation between a point found in the RGNIR frame to the pixel location in thermal space (Eqn. 2.7). However, this representation is simplified as it does not take into account rotational differences in the camera mount and assumes the optical centers of both the camera are aligned. A generalized form of Eqn. 2.7 is given in Eqn. 2.8 where the rotational ($\mathbf{R}^T_{NIR}$) and the translation alignment errors between the camera optical centers ($\mathbf{T}^T_{NIR}$) are included.

$$\begin{bmatrix} \mu_T \\ \nu_T \\ 1 \end{bmatrix} = \frac{1}{Z} \mathbf{K}_T \left(\frac{\mathbf{K}_{NIR}}{Z} \right)^{-1} \begin{bmatrix} \mu_{NIR} \\ \nu_{NIR} \\ 1 \end{bmatrix} \tag{2.7}$$

$$\begin{bmatrix} \mu_T \\ \nu_T \\ 1 \end{bmatrix} = \frac{1}{Z}\mathbf{K}_T \left(\mathbf{R}_{NIR}^T \left(\left(\frac{\mathbf{K}_{NIR}}{Z} \right)^{-1} \begin{bmatrix} \mu_{NIR} \\ \nu_{NIR} \\ 1 \end{bmatrix} \right) + \mathbf{T}_{NIR}^T \right) \tag{2.8}$$

In an ideal mounting scenario, the translation and rotation alignment between the two cameras can be calibrated beforehand and remain constant during flight. Assuming the physical restraint of the cameras remain the same, and the cameras have confident intrinsic calibrations, Eqn. 2.8 can be used to determine the accuracy of a given image synchronization.

The KHawk-55T cameras are stabilized by foam blocks in the 2019 fire flight. In addition, the strong wind during the flight ($\sim$12-15 mph) and reactionary adjustment from the sUAS caused the cameras to move slightly mid-flight, which then changed the viewing angle of the thermal and RGNIR images multiple times. During straight legs of the flight path, the PeauPro82 GoPro would maintain a constant viewpoint. During periods of turbulence or high roll turns, the camera would jostle in the payload bay. While coverage of the ground would be about the same, the slight movement would change the alignment between the PeauPro82 and the FLIR Vue Pro R. A significant amount of turbulence occurred midway through the flight, causing the PeauPro82 to pitch down. As shown in Fig. 2.8a, the RGNIR image was already "behind" the thermal image (Fig. 2.8b) as the fire in the center of the thermal image is at the top of the RGNIR image. After the midway point of the flight, the overlap between the PeauPro82 and the thermal image was only a few pixels and fire coverage in the overlap was minimal. Therefore, a single estimate of the rotation matrix between the PeauPro82 and the FLIR Vue Pro R would not work for this dataset.

For the GRAFFITI dataset overlay comparison, each image was matched on an individual basis by estimating the transformation between the RGNIR image to the thermal image space. At the altitude flown, the FLIR Vue Pro R and the PeauPro82 had a spatial resolution of 0.23 $^{m}/_{pix}$ and 0.094 $^{m}/_{pix}$, respectively. The PeauPro82 RGNIR images were down sampled to the thermal image space to have the same spatial resolution for comparison.

The problem of transforming the RGNIR image to the thermal image space is defined as a projective transformation problem in computer vision; the general equation for mapping a point on

the same plane from two different view-points ($\mathbf{x} \rightarrow \mathbf{x}'$) is given in Eqn. 2.9 [18]. For estimating the transformation between points found in the RGNIR image ($\mathbf{x}_{NIR}$) to the thermal space ($\mathbf{x}_T$) , Eqn. 2.10 can be used. At the altitude flown (120 m AGL) and the relatively flat landscape flown over, the shared points between the two images can be assumed to be on the same plane and therefore can utilize existing optimization algorithms from the two-view geometry problem in literature.

$$\mathbf{x}' = \begin{bmatrix} x_1 \\ x_2' \\ x_3' \end{bmatrix} = \begin{bmatrix} h_{11} & h_{12} & h_{13} \\ h_{21} & h_{22} & h_{23} \\ h_{31} & h_{32} & h_{33} \end{bmatrix} \begin{bmatrix} x_1 \\ x_2 \\ x_3 \end{bmatrix} = \mathbf{H}\mathbf{x} \tag{2.9}$$

$$\mathbf{x}_T = \begin{bmatrix} \mu_T \\ \nu_T \\ 1 \end{bmatrix} = \begin{bmatrix} h_{11} & h_{12} & h_{13} \\ h_{21} & h_{22} & h_{23} \\ h_{31} & h_{32} & h_{33} \end{bmatrix} \begin{bmatrix} \mu_{NIR} \\ \nu_{NIR} \\ 1 \end{bmatrix} = \mathbf{H}_{NIR}^{T}\mathbf{x}_{NIR} \tag{2.10}$$

The level 1 GRAFFITI dataset consists of 20 paired thermal and RGNIR images. The pairs considered needed to include significant portions of the fire front as well as enough features visible in both images that can provide enough information to estimate the homography between the RGNIR and thermal images. The full criteria for choosing an image in the GRAFFITI dataset are:

1. The fire front appears in the shared field of view of the thermal and RGNIR images;
2. Distinct features (field corners, vehicles, roads, etc.) are shared in both images;
3. Roll and pitch angles are less than 20 degrees.

The roll and pitch criteria are used to limit the image distortion when reprojecting the RGNIR and thermal images for georeferencing. The GRAFFITI dataset is intended for fire metric analysis from different spectral bands which may involve georeferencing. Besides yaw, when a downward facing camera on an aircraft has an attitude angle above 20 degrees, georeferenced images require homographies that overly distort the image and affect the georeferencing accuracy [19]. The statistics for the roll and pitch angles for the GRAFFITI dataset are shown in Table 2.4 derived from the Pixhawk IMU datalog.

Table 2.4: Roll and pitch statistics for GRAFFITI dataset.

Attitude Angle	Range (deg.)	Mean (deg.)	Standard Deviation (deg.)
Roll (ϕ)	(-16.46 - 4.29)	-6.53	11.27
Pitch (θ)	(1.71 - 10.10)	6.16	2.58

The FLIR Vue Pro R was set to high-gain mode to have the ability to provide distinct environmental features for georeferencing, which can also be used to pair with the RGNIR images. The manually selected features in both images include field corners, vehicle corners, ground station features, and hay bales. Two example image pairs with defining features that include the fire perimeter in different areas at different times are shown in Fig. 2.9. The relative size between the images in Fig. 2.9 are resized for visualization purposes.

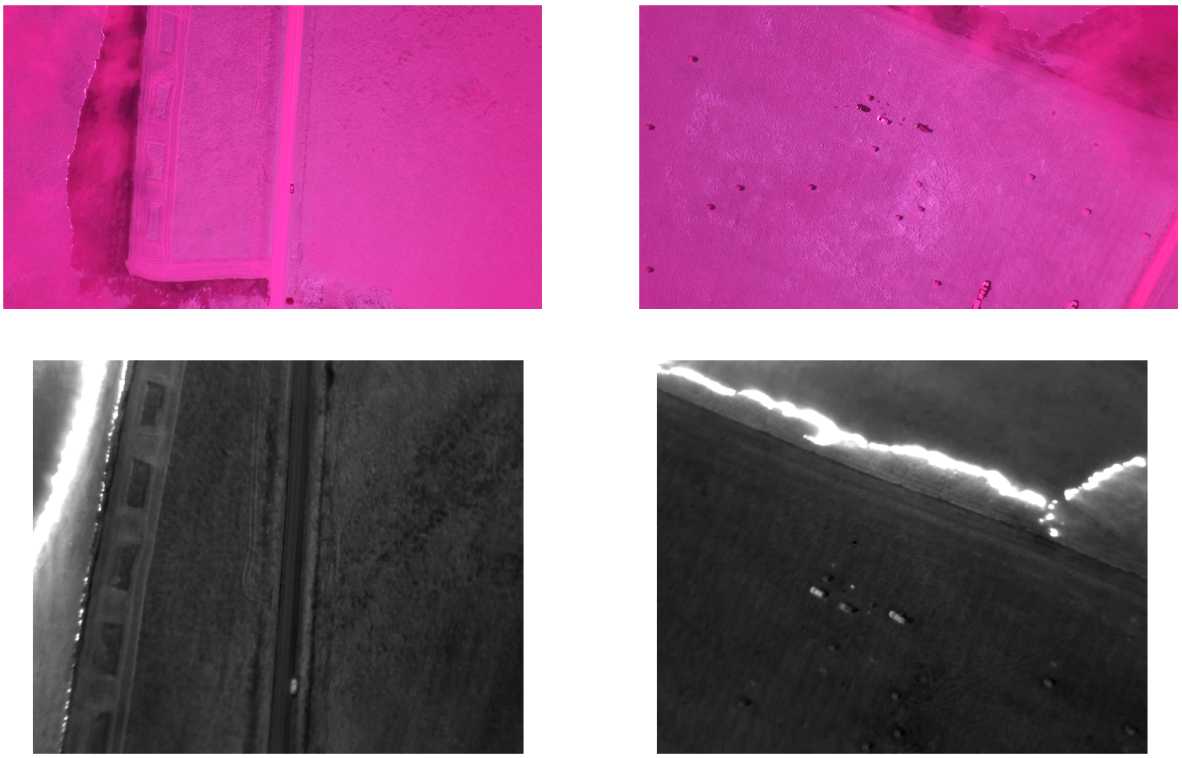

Figure 2.9: Resized RGNIR and thermal image pairs from the GRAFFITI dataset (Taken at 12:10:14 PM (left) and 12:13:40 (right).

The projective transformation matrix shown in Eqn. 2.10 has eight degrees of freedom, since the matrix is defined up to scale. Therefore, at least four features in the thermal and RGNIR images need to be matched to estimate a homography. With four matched features, an exact solution for Eqn. 2.10 can be determined. Correspondences with more than four points can potentially provide a more accurate representation of a projective transformation, however further optimization is required. After manually identifying and matching features for the 20 images in the GRAFFITI dataset, the M-estimator SAmple Consensus (MSAC) algorithm was used with a 99.9% confidence of finding the maximum number of inliers for estimating a projective transformation. The MSAC algorithm improves upon the RANSAC estimator by maximizing the likelihood of the homography solution rather than the number of inliers present in a given homography [20].

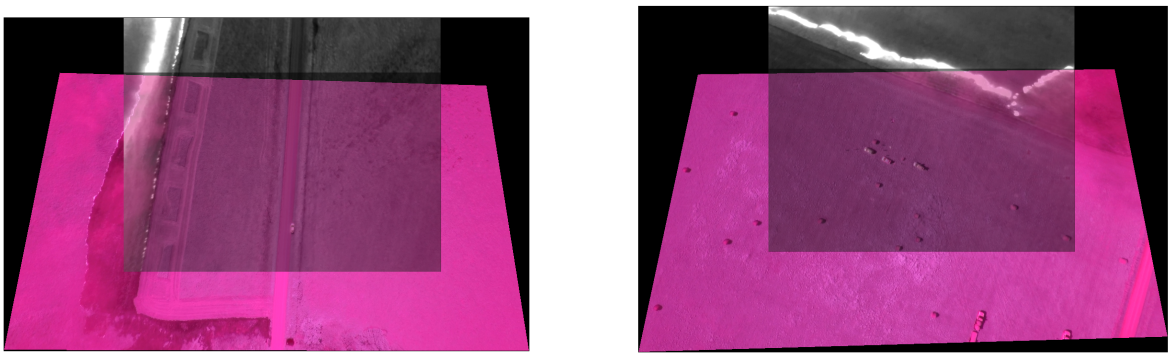

Figure 2.10: Overlays from the GRAFFITI dataset examples shown in Figure 2.9.

Fig. 2.11 presents the reprojection error for the 20 images in the original GRAFFITI dataset along with the feature point distribution in the thermal image. Reprojection error refers to the distance between a point identified in the thermal image to the RGNIR point projected in the thermal space. The lower the projection error often represents a more accurate homography estimate. The feature distribution within the image is also critical to the estimation accuracy. If all the matched features within an image are tightly packed, small deviations in homography estimates may create warped overlays even when the reprojection errors are small. Feature distribution (Eqn. 2.11) is defined as the root-mean-square Euclidean norm of the distance between the i-th feature location (x_i) and feature centroid (μ_x) of an image for N features in an image.

$$FD = \sqrt{\frac{\sum_{i=1}^{N} \|x_i - \mu_x\|}{N}} \tag{2.11}$$

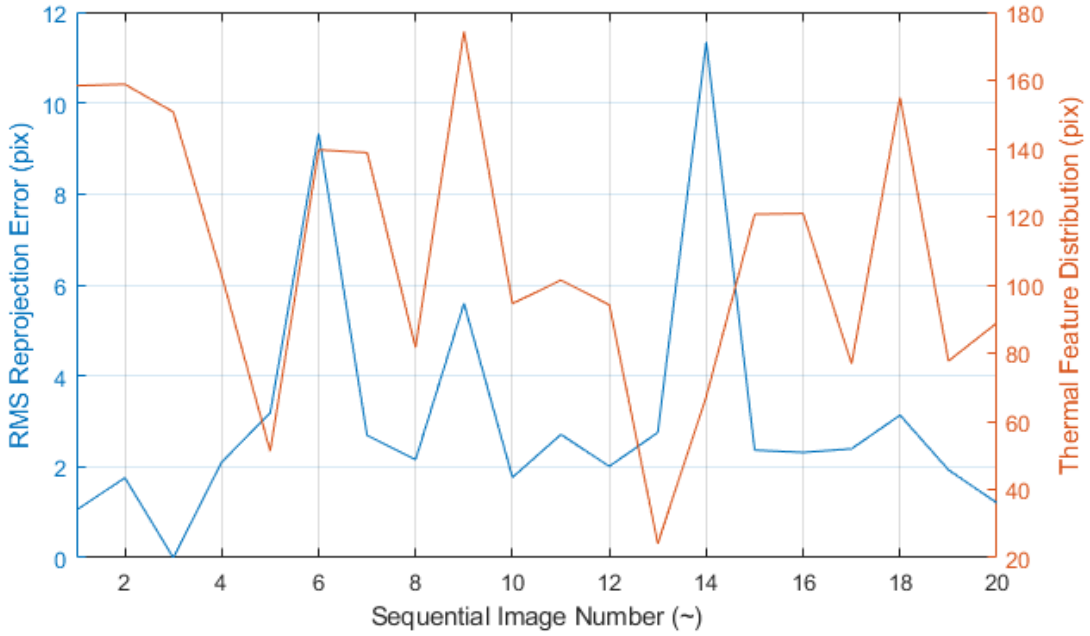

Figure 2.11: Reprojection error and feature distribution for the original GRAFFITI dataset homography estimation.

As clearly shown in Fig. 2.11, image 14 of the original GRAFFITI sequence has a large reprojection error and relatively low feature distribution (∼60 pix). The manually selected features (yellow dots) and RGNIR reprojected points (red dots) on the thermal image are shown in the top image of Fig. 2.12. While there are more than the required four matched features, the close proximity causes the estimator to exclude two outliers (right most features). While having minimal reprojection error, that minor deviation paired with the tight grouping causes the reprojected overlay to over-exaggerate the estimated homography and create an unusable overlay image, shown in the bottom image of Fig. 2.12.

Images from the GRAFFITI dataset that produce accurate overlay comparisons would consist of a wide distribution of features with a low reprojection error. Using the results from Fig. 2.11, Table 2.5, and visual inspection, 15 images from the original 20 were determined to have acceptable homography estimates based on an RMS reprojection error less than five pixels and a feature

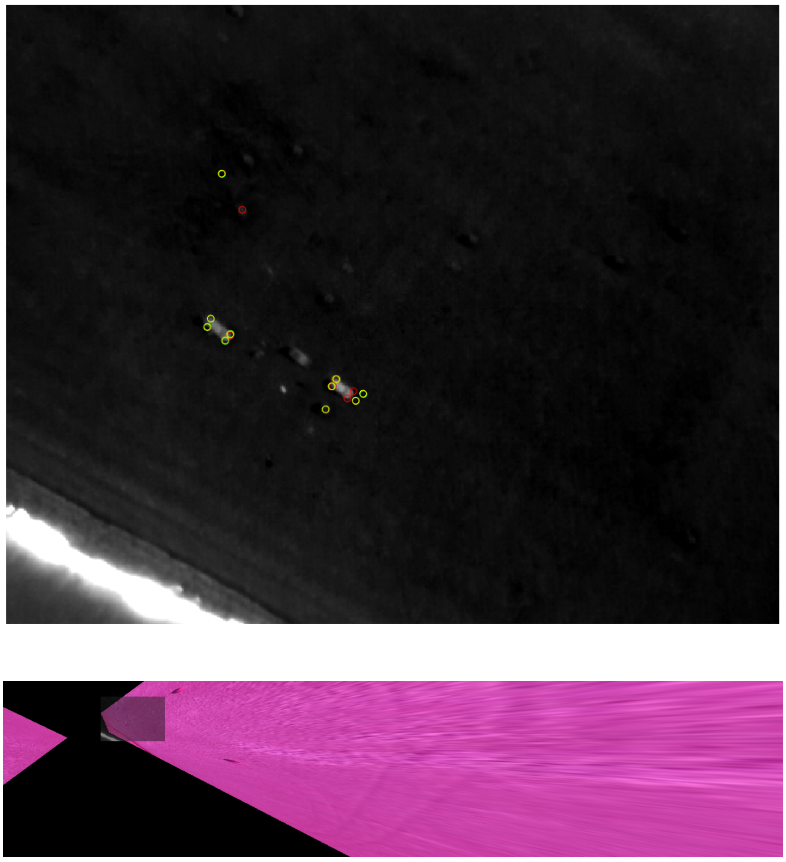

Figure 2.12: Tightly packed identified features (yellow) with respective reprojections (red) on the thermal image (top) with the estimated homography overlay (bottom).

distribution greater than 80 pixels. Statistics of the chosen 15 image dataset are shown in Table 2.5. The final level 2 GRAFFITI dataset has a reduced average reprojection error by a pixel and half the original standard deviation when compared to level 1. The feature distribution is more favorable with an average 10 pixels higher and less spread than the original 20 image dataset.

Table 2.5: Reprojection error and feature distribution statistics of the original and trimmed GRAFFITI dataset.

Parameter	Reprojection Error [Original]	Feature Distribution [Original]	Reprojection Error [Trimmed]	Feature Distribution [Trimmed]
Mean (pix)	3.09	108.89	2.17	121.28
Standard Deviation (pix)	2.72	40.47	1.26	33.53

Although this is a relatively small dataset, the RGNIR and thermal image overlays from the nadir perspective of a low altitude sUAS are unique in the existing literature of wildland fire observation. This high resolution 15 image dataset provides not only raw RGNIR and thermal images of a controlled grass fire front, but overlays of both images that can be potentially used for further fire metrics measurements (fire front detection and localization, rate of spread, fire front delineation, flame zone depth analysis) between the two spectrum representations.

The GRAFFITI dataset consists of 70 images in total: 20 thermal and RGNIR image pairs (level 1) as well as 15 overlays between selected image pairs (level 2). A majority of the image processing performed in this section relied upon manual oversight and adjustment. Future implementations of the KHawk-55T and other sUAS carrying similar imaging payload would require rigid camera mounting that can maintain the same alignment across multiple flights. This would allow for a single calibration process to be performed that would be consistent and repeatable.

2.4 Conclusions

This chapter described the acquisition and development of the GRAFFITI dataset which includes a total of 20 level 1 RGNIR and thermal image pairs over typical tall-grass Fall fires in Kansas. Images were chosen based on low attitude angles, pertinent features in frames and good representation of fires. The GRAFFITI dataset also consists of a selection of 15 overlays (level 2) with a reprojection error of 1.26 pixels (roughly 10 cm) with a feature distribution of 121 pixels. GRAFFITI provides fire front imagery in the RGNIR and thermal spectrum to support further comparison of grass fires in different spectrums. Later chapters will use the dataset for fire behavior metric measurements. For future sUAS imaging data collection, a hard-mounted payload configuration is highly recommended for a consistent transformation estimate between different cameras to create larger image sets over multiple flights.

Chapter 3

Rule-based Grass Fire Front Identification Using sUAS NIR Imagery

3.1 Chapter Introduction

This chapter focuses on the development of a new grass fire front identification method using sUAS NIR aerial imagery. Existing fire detection methods generally use rule-based image processing algorithms in different color spaces including RGB [21, 22], YUV [23], YCbCr [24] and combinations of other spaces [25]. Additionally, most methods use imagery taken from the ground [26], staring at cross-section of the fire, or from angled aerial views, obscuring sections of the fire perimeter [27]. These visible spectrum-based methods may not work well in nadir conditions when omitting smoke impact or in situations with minimal contrast between a background that is bright and produces a high intensity region that is not fire (i.e. sky and smoke). Accurate airborne assessments of wildland fires require higher resolution imaging than most free satellite datasets offer, therefore this task would rely on nadir images taken from an sUAS that can capture a wider view of fire areas [28]. This chapter proposes a novel fire detection and fire front identification algorithm using sUAS nadir imagery taken in the red, green and near-infrared (NIR) spectrum. Fire detection using the NIR spectrum has been done using satellite images, but are designed for large land areas that produce results at a spatial resolution in the hundreds or thousands of kilometers per pixel [29, 30].The NIR imagery used in this chapter has a higher spatial resolution than the ones used in literature, which have not been fully tested in airborne and nadir situations.

3.2 Existing Rule-based Methods for Fire Detection

A supervised learning-based algorithm is proposed for fire detection using a 3-channel RGB histogram to determine fire pixels [21]. To increase the probability of fire pixel detection, a Gaussian-based approach is used after an initial learning process. Using the $256 \times 256 \times 256$ pixel histogram of the output image, a Gaussian filter is applied to the image. When pixels are determined as a "correct" fire pixel (a mask location with a binary value of "1"), a Gaussian distribution is added to the color histogram. If the pixel was not determined to be fire, a small negative Gaussian distribution is applied. This method attempts to mitigate color invariances due to burning material and environment variance. However, the algorithm will not perform well if similar colors appear in the back and foreground, since this method relies on color response by thresholding a Gaussian-smoothed color histogram. The smoothing aspect does alleviate the motion component of the fire when against backgrounds of a similar color.

A widely used fire detection procedure was proposed utilizing the RGB and saturation (S) color spaces [22]. The efficiency and speed of this method comes from its easy detection of fire in the red to yellow spectrum of color. For fires, the red channel response is higher than the green channel response, and respectively the same for the green to blue channel. Finally, since fire essentially acts as a lighting source, the red channel values can be easily detected using a customized threshold. These methods are shown below where I_R, I_G, I_B are the red, blue and green channel intensities at the pixel location (u,v). A pixel is determined to be fire if the $r_{1,\,[22]}$, $r_{2,\,[22]}$, and $r_{3,\,[22]}$ are all greater than zero.

$$r_{1,\,[22]}(u,v) = I_R(u,v) - I_G(u,v) \tag{3.1}$$

$$r_{2,\,[22]}(u,v) = I_R(u,v) - I_B(u,v) \tag{3.2}$$

$$r_{3,\,[22]}(u,v) = I_R(u,v) - \tau_R \tag{3.3}$$

The proposed rule set includes the saturation channel (I_S) to remove regions of an image that have high background illumination. With the rule given below, the two tunable thresholds on the

red and saturation channel, τ_R and τ_S respectively, will change based on the color profile of the fire image dataset.

$$r_{4,\,[22]}(u,v) = I_S(u,v) - (255 - I_R(u,v))\frac{\tau_S}{\tau_R} \tag{3.4}$$

Another RGB image-based method is proposed in [24] similar to [22] in using the same red, blue and green channel comparisons. Instead of using a threshold on the red channel, the mean red channel response of the image, $I_{R,mean}$, is selected as an indicator of fire:

$$r_{1,\,[24]}(u,v) = I_R(u,v) - I_{R,mean} \tag{3.5}$$

Other fire detection methods use the YCbCr (luma, blue chrominance and red chrominance) color space for the separation between intensity and chrominance of fire is more distinguishable. Similar rules are provided for the YCbCr (luma, blue chrominance and red chrominance) color space [24], implying that the luminance and red chrominance are greater than the blue chrominance for fire pixels. This is a more robust approach to represent fire pixels as the chrominance is used in modeling color instead of intensity, which caused illumination issues in the RGB color space.

$$r_{2,\,[24]}(u,v) = I_Y(u,v) - I_{C_b}(u,v) \tag{3.6}$$

$$r_{3,\,[24]}(u,v) = I_{C_r}(u,v) - I_{C_b}(u,v) \tag{3.7}$$

To further segment the image in YCbCr space, since the fire region of an image will usually be the brightest in an image, the mean values for each channel intensity were used. For fire, Celik determined that the Y channel will be greater than the average luminance, while the blue chrominance channel will be smaller than the mean. And since the red channel for fire is saturated, the red chrominance will be greater than the average. These rules are shown below in Equations 3.8 - 3.10.

$$r_{4,\,[24]}(u,v) = I_Y(u,v) - I_{Y,mean} \tag{3.8}$$

$$r_{5,\,[24]}(u,v) = I_{C_b,mean} - I_{C_b}(u,v) \tag{3.9}$$

$$r_{6,\,[24]}(u,v) = I_{C_r}(u,v) - I_{C_r,mean} \tag{3.10}$$

Another method for detecting fire is using a probabilistic approach [31]. Each channel of the RGB color space is modeled using a Gaussian distribution of probability (Eqn. 3.11). This method attempts to mitigate the use of multiple empirical thresholds, which can fail when the combusted material or the background environment changes.

$$p_C(I_C(u,v)) = \frac{1}{\sqrt{2\pi\sigma_C^2}} \exp\left(-\frac{(I_C(u,v) - \mu_C)^2}{2\sigma_C^2}\right) \tag{3.11}$$

where $c \in [R,G,B]$ and μ, σ^2 are the corresponding mean intensity and variance for each channel, respectively. The overall probability for a pixel distribution within an image can be estimated using Eqn. 3.12. The determination of a fire pixel can be finished using a threshold, τ_K, on the overall probability (Eqn. 3.13).

$$p_r(I(u,v)) = \prod_{c \in [R,G,B]} p_C(I_C(u,v)) \tag{3.12}$$

$$r(u,v) = p_r(I(u,v)) - \tau_K \tag{3.13}$$

The methods and rules described section 3.2 are mostly designed for ground-level fire detection. For the application of fire detection from sUAS aerial imagery, the relative size of the fire can be drastically smaller and dependent on the pixel resolution of the image, where thin portions of a fire line can be imperceptible. The test images used in the above detectors contain large portions of fire, therefore application of these methods to sUAS imagery of a grassland fire will not detect thinner fire fronts from a nadir perspective. Additionally, the above methods do not consider occlusion from smoke, which often is between the fire and nadir sUAS imagery. Attempting to mitigate these issues, a new methodology for fire detection using the intrinsic properties of the NIR spectrum is proposed in this chapter.

3.3 NIR Response to Fire

Near infrared cameras can detect radiating bodies (such as fire) with an improved sensitivity when compared to RGB solutions. Simulations have shown that the radiance response from high temperature areas are more detectable in the NIR range than a human eye or a visual spectrum camera can sense [5]. Figure 3.1 presents an example RGNIR image from the Anderson County prescribed fire, along with the red, green and NIR single channel images. Fire pixels can be easier observed in the NIR imagery than typical visible spectrum cameras due to the improved contrast between the background and fire, and reduced occlusion effect due to smoke. It can be observed in the red (Fig. 3.1b) and NIR (Fig. 3.1d) image channels that fire produces a high intensity response, while the smoke visible between the images is less in the NIR image. The fire front at the left of the image has hot spots clearly visible in the NIR channel, but the red channel image introduces a smoke response which obscures and covers the thin fire region. It is also noted that the green channel image (Fig. 3.1c) also shows the leftmost fire front hot spots.

3.4 Proposed NIR Fire Detection Method

The proposed NIR fire detection method in this section produces two separate images: the detected fire pixels and a fire front line representation. The algorithm uses a raw RGNIR image and creates four images: the single channel red, green and NIR images as well as a difference image between the red and NIR channel. Using mean channel characteristics, Gaussian histogram assumptions and thresholding, Eqn. 3.14 - 3.16 were developed and consist of the rule-based section of the algorithm that determines initial fire pixels (Sec. 3.4.1). False positive pixels outside the fire area are eliminated by detecting the burnt region of the image (Sec. 3.4.2). If the potential fire pixel is near the detected dark region, it passes as a final fire pixel. To convert the fire pixel image into a format for further analysis, a fire front representation is created through morphological processing (Sec. 3.4.3). The full fire detection algorithm is summarized in Fig. 3.2.

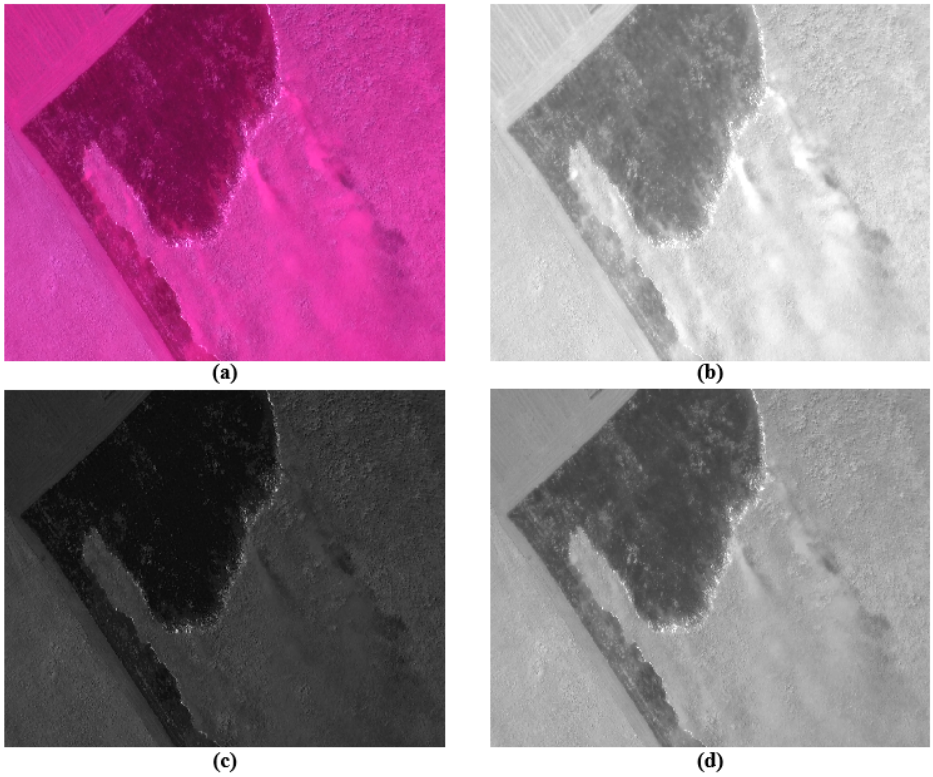

Figure 3.1: RGNIR image of a fire line (a) and the separate channel responses: red (b), green (c) and NIR (d) (12:14:14 PM).

3.4.1 RGNIR Fire Detection Rules

A new algorithm is proposed for the detection of fire pixels in the aerial RGNIR imagery, which is comprised of three rules. The first rule proposed for detecting candidate fire pixels is based on a Gaussian histogram approach similar to [21, 31]. The rule shown in Eqn. 3.14 defines any pixel above two standard deviations of the NIR channel (σ_{NIR}) mean response ($I_{NIR,mean}$) as a candidate fire pixel. Based on results from [5], the rule shown in Eqn. 3.14 will theoretically catch any unoccluded fire pixel from the high response caused by the fire's high radiance in the NIR spectrum. Similar to other rule-based methods, a pixel is determined to be a fire pixel candidate if the rule provides a value above zero.

$$r_{NIR,1}(u,v) = I_{NIR} - (I_{NIR,mean} + 2\sigma_{NIR}) \tag{3.14}$$

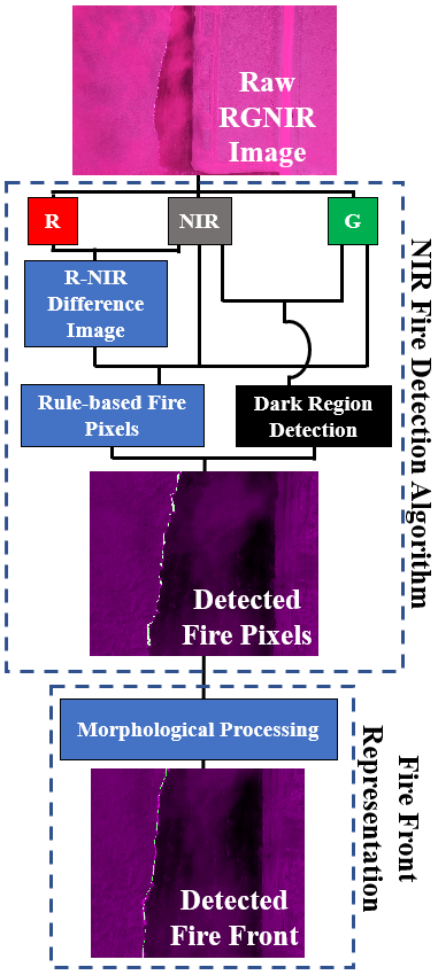

Figure 3.2: NIR fire detection algorithm flow chart.

Due to varying levels of smoke present during wildfire situations, a majority of the fire front will be occluded by airborne particles. For further identification of fire that does not directly maximize the response in the NIR-band, an absolute value process was chosen similar to Eqn. 3.5 [24]. Since fire will still have a relatively high intensity response in the NIR and red channels, subtracting the two images will draw the fire areas towards zero. However, other occlusions or objects within the image, which have different intensities between the NIR and red channels will be clearly seen in the difference image. By using the mean pixel intensity of this image (Fig. 3.3) it is shown that the areas of high red response, the gravel road and smoke in this case, are clearly seen while the fire line is not visible. The difference image can then be used to find additional candidate fire pixels

that were not easily found using Eqn. 3.14. The rule is summarized in the equation below.

$$r_{NIR,2}(u,v) = -\left|I_R(u,v) - I_{NIR}(u,v)\right| + I_{R-NIR,mean} \tag{3.15}$$

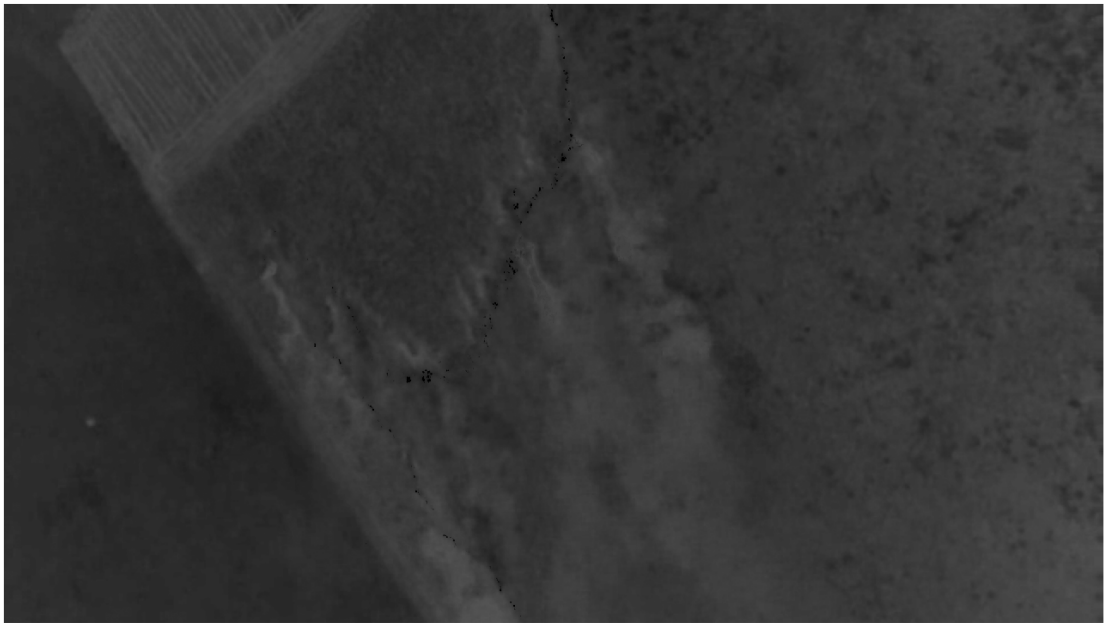

Figure 3.3: Red and NIR channel difference image.

However, for the resulting image, areas that have similar intensities in both the NIR and red channels will produce the same result as a fire pixel. While this includes the fire line, regions of burnt material or consistently dark regions will also be able to pass through as a candidate pixel. Therefore, an additional rule is proposed in Eqn. 3.16. Fire will still produce a high green channel response, while dark areas will not. A basic thresholding method is added for its simplicity and speed of computation [22]. For the dataset used in this paper, the threshold for the green channel was chosen as $\tau_G = 179$, roughly 70% of the maximum green channel intensity.

$$r_{NIR,2}(u,v) = I_G(u,v) - \tau_G \tag{3.16}$$

The result of the three above rules are shown using the test image shown in Figure 3.4 as

a binary image where fire pixels are defined as “1” and all other pixels are “0”. Figure 3.4 was cropped to present a less compressed version of the full image results. As shown, Figure 4 excludes the burnt areas that were considered candidate pixels using the absolute value method (Eqn. 3.15). Likewise, the high red channel responses of the smoke and gravel road are omitted as well.

Figure 3.4: Resulting cropped binary image fire pixels of Figure 3.1 using proposed fire detection algorithm.

3.4.2 Dark Region Detection

Figures 3.1 and the resulting fire pixel detection image (Fig. 3.4) show an ideal fire front image. The fire is in the center of the image and it includes some occlusion due to smoke, but there are instances during flight where the fire is only part of the image and the landscape or other objects are in the majority of the frame. Since the rules above rely on an intense response in the NIR, red and green channel, a scene with few fire pixels can cause many false positives. An example of an unideal image with fire present is shown in Figure 3.5a. While fire is present in the lower left corner of the image, the majority of the frame includes open field, haybales and wild brush. Figure

3.5b presents the results of the first three proposed rules when applied to the unideal image, which indicates fire is in the frame but mislabels pixels near the gravel road as well as some sections of the open field that produced high intensities in the red, green and NIR channels. This occurs when a large amount of high intensity pixels are missing in the image histogram (usually caused by fire), which allows some high intensity sections of the image to be considered as fire.

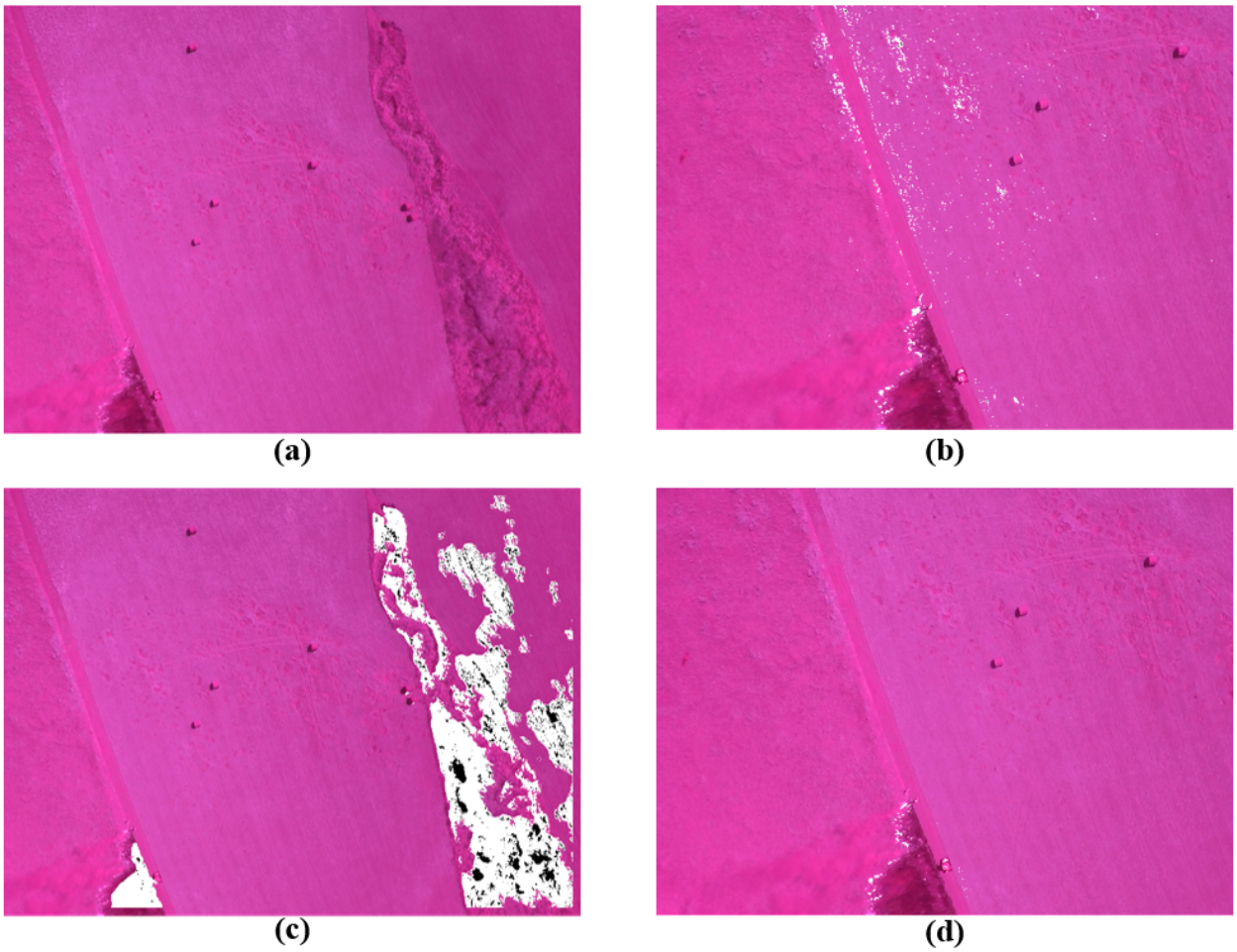

Figure 3.5: Unideal fire front image scenario (a) with initial fire candidate pixels [white] (b), dark region identification [white] (c) and final fire candidate pixels [white] (d).

To eliminate these false positives, a basic detector for finding dark regions of the image can be used. The outlier pixels that are mislabeled as fire are far away from the current fire front and therefore not near the burning region or the burnt vegetation that the fire has already passed through. Therefore, reasoning similar to the logic used in Eqn. 3.14 can be borrowed to find dark regions within an image. The proposed burnt region detector is shown below in Equations 3.17

and 3.18. Only the green and NIR channels are chosen as NIR will mitigate most smoke coverage while the green channel is included to attempt and mitigate other vegetation present in the sUAS imagery.

$$r_{dark}(u,v) = (I_{G,mean} - 2\sigma_G) - I_G(u,v) \tag{3.17}$$

$$r_{dark}(u,v) = (I_{NIR,mean} - 2\sigma_{NIR}) - I_{NIR}(u,v) \tag{3.18}$$

While a majority of the burnt regions in frame can be detected, smoke can brighten the dark areas and cause cavities within larger burnt areas or completely miss edges of the burnt vegetation. Therefore, to conglomerate the dark regions to a single area, a burnt region identifier similar to the edge detector proposed in [32] is proposed. Features from Accelerated segment Test (FAST) was designed to be fast and efficient for machine learning applications. Using a circular perimeter of pixels around a potential edge within an image, the pixel is determined as a corner if a certain number of pixels within the perimeter are higher or lower than the candidate pixel and a given intensity threshold. If 75% of the observed pixels fall outside of the intensity range, the pixel is determined as an edge. For the purpose of dark area detection, a box filter with a width of 20 pixels is used to go over the image after identifying dark pixels. If over 75% of the filter is considered dark, the candidate pixel at the center of the filter is considered dark as well. Figure 3.5c presents an unideal image after using the detector, with the dark regions shown in white.

Given that candidate fire pixels will be on or near to the determined dark regions, ideally near burnt vegetation, a candidate fire pixel is determined to be part of the fire front if it is within 5 meters (25 pix) of the dark regions. The false positives due to a high intensity and low fire coverage within the image will be eliminated as fire, as those pixels will not be near other dark regions of the image such as forested areas.

3.4.3 Morphological Processing

To create a continuous fire front representation from the algorithm results, a morphological process involving image dilation and erosion was used. The original output from the fire detection

algorithm produces pixel locations where fire was determined to be, however due to the controlled nature of the burn and sensitivity of the algorithm, there are areas between fire pixels where smoke occluded a bright fire location. Additionally, the initial fire front had periods of low flaming combustion causing gaps between highly active sections of the fire and from the low intensity response from the PeauPro imagery.

Image dilation is performed on binary images for the purpose of extending the boundary of a foreground region. A fire pixel will become a larger shape in the case of the fire detection algorithm. To create a fire front representation from the binary algorithm output image, morphological dilation using a disk structure was applied to the image to connect all the detected fire pixels and fill gaps left in the algorithm process. Shown on an example fire image in Figure 3.6b, the disk structural element was chosen as the algorithm does not determine the primary fire front direction. While fire fronts have a general direction of spread, the quasi steady state of the fire can cause bumps and grooves in the fire front line. A circular shaped element will allow for a dilation size that is unbiased in any single direction, while a rectangular element may generate a bias along the principle direction of a rectangular element instead of the true geometry of the fire front.

The dilated representation of the fire captures the overall geometry of the fire perimeter, however areas in front of and behind the fire provide a false number of fire pixels in an image, as expected. Image erosion, referred to as morphological filtering [33], is used to create a pixel-wide "line" that can be used as a representative fire front produced from the original NIR image. After the dilation process connects the gaps between the detected fire pixels, erosion will create a single pixel line that maintains the original "medial axis" of the dilated pattern [34]. Referred to as skeletonization, an erosion process was applied to each dilated image (Fig. 3.6b) of the image set and a final fire front line was produced for each fire image. The erosion process results are shown on the test image (Fig. 3.6a) in Figure 3.6c.

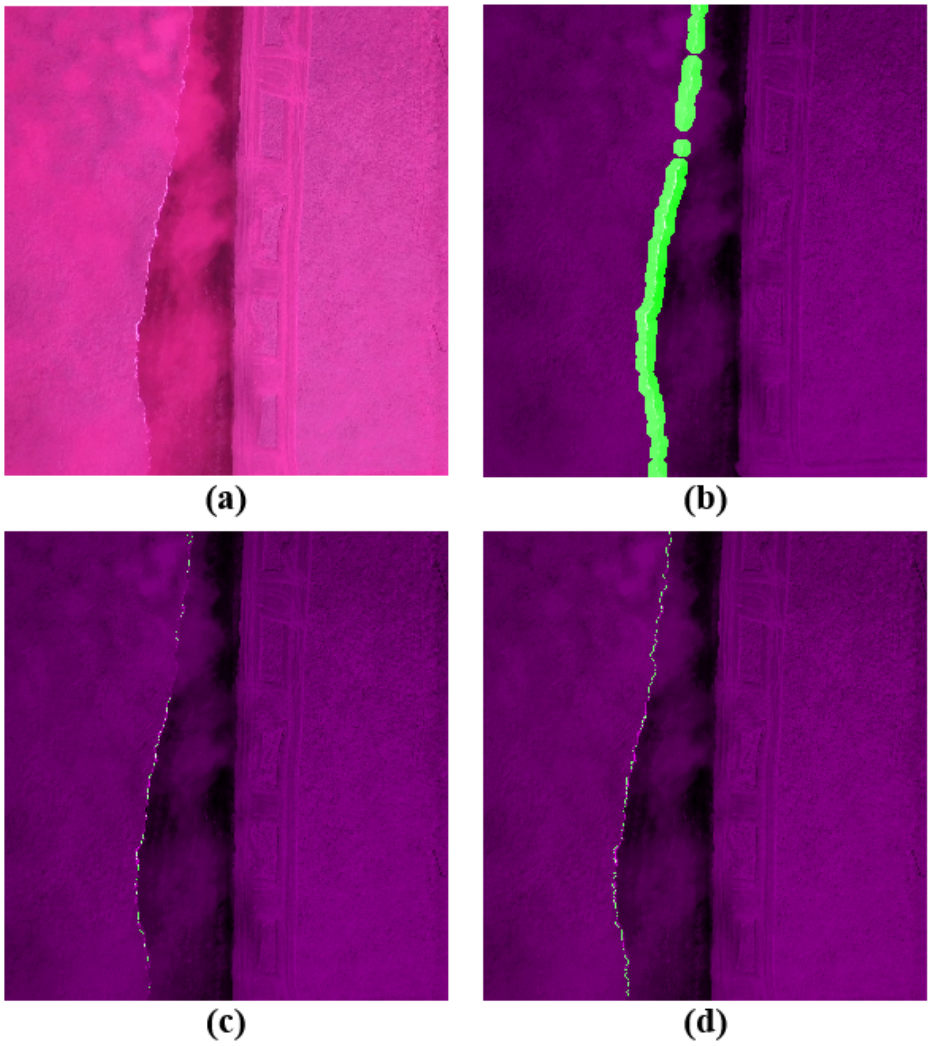

Figure 3.6: RGNIR image under morphological dilation with diamond element (b), thinned erosion (c) and the manually labeled ground truth image (d) (12:10:15 PM).

3.5 Evaluation Criteria and Results

For evaluating the accuracy of the rule-based NIR fire detector discussed in this chapter, it is desired to have a ground truth representation of the fire front as well as a front developed from the fire pixels determined from the algorithm. By comparing the location and length of a manually labeled fire front and the front produced by the NIR algorithm, quantitative assessment can be performed using the Pratt Figure of Merit (PFOM).

The ground truth used for comparison (Fig. 3.6) was taken from the 20 NIR image set from the level 1 GRAFFITI dataset described in Chapter 2. The ground truth line was generated by manually

delineating the fire front in each image and creating a binary map of the fire front location. For the test image used as an example in Section 3.4.3, the manually labeled ground truth fire front line is shown in figure 3.6. As shown, while sections of the fire front have gaps in the eroded image (Fig. 3.6c), the produced line follows the fire front and captures the geometry of the front closely.

To compare the algorithm detected fire front and the manually labeled ground truth, certain metrics need to be selected similar to edge detection evaluation. The Pratt Figure of Merit (PFOM) is proposed for use as an edge detection evaluator [35] where the primary errors in detection are fragmentation, offset differences and smearing, which are all present in the NIR fire front dataset when compared to the ground truth line. Shown below in Eqn. 3.19, the PFOM takes into account the number of pixels in the fire front of the ground truth (I_{gt}) and the algorithm estimate (I_{alg}), the mean squared distance of the k-th pixel detected to the closest pixel in the ground truth image, and a scaling constant of $\alpha = \frac{1}{9}$. The constant was chosen to relatively penalize thickened lines and offset, isolated pixels, as used in other edge detection evaluations [35, 36]. The cardinality of the ground truth and the algorithm estimate refers to the amount of fire pixels contained within each image. In edge detection applications, the PFOM of various edge detectors ranges from 0.4 - 0.6 for simple edge detectors while more advanced and computationally expensive detectors can reach above 0.7 [37].

$$PFOM(I_{gt}, I_{alg}) = \frac{1}{max\{card(I_{gt}), card(I_{alg})\}} \sum_{k=1}^{card(I_{gt})} \frac{1}{1 + \alpha d^2(k)} \tag{3.19}$$

The PFOM with cardinality difference between the ground truth and algorithm results of each sequential image taken from the overlapped data set created in Chapter 2 is shown in Figure 3.7. With an RMS value of 0.54 over the 20-image set, the algorithm described above is comparable to the basic edge detectors evaluated in the literature using the same figure of merit. Images that generated a high PFOM showed the fire front throughout the image, including portions where smoke is occluding the front (Fig. 3.8). However, if the fire perimeter is heavily occluded, the image contains highly reflective objects, or the fire front is barely in frame, the NIR algorithm may produce false positives or miss sections of the fire.

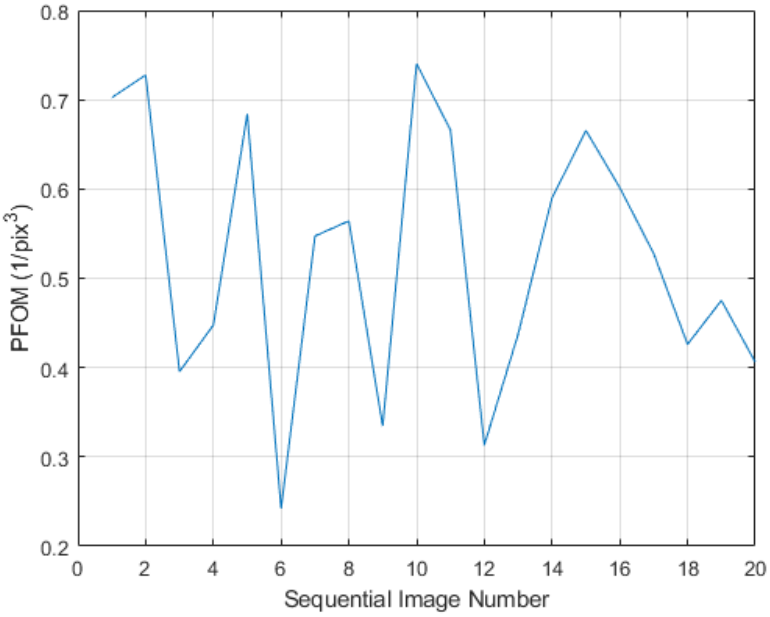

Figure 3.7: Pratt Figure of Merit results for the NIR dataset

Figure 3.8a represents an ideal image for representing the fire perimeter using the NIR algorithm. While the fire front is thin and covered by smoke, the NIR band was able to detect occluded fire pixels. As shown in Figure 3.8b, the morphological processes of the algorithm developed a fire front representation (purple) that followed the manually labeled ground truth line (green).

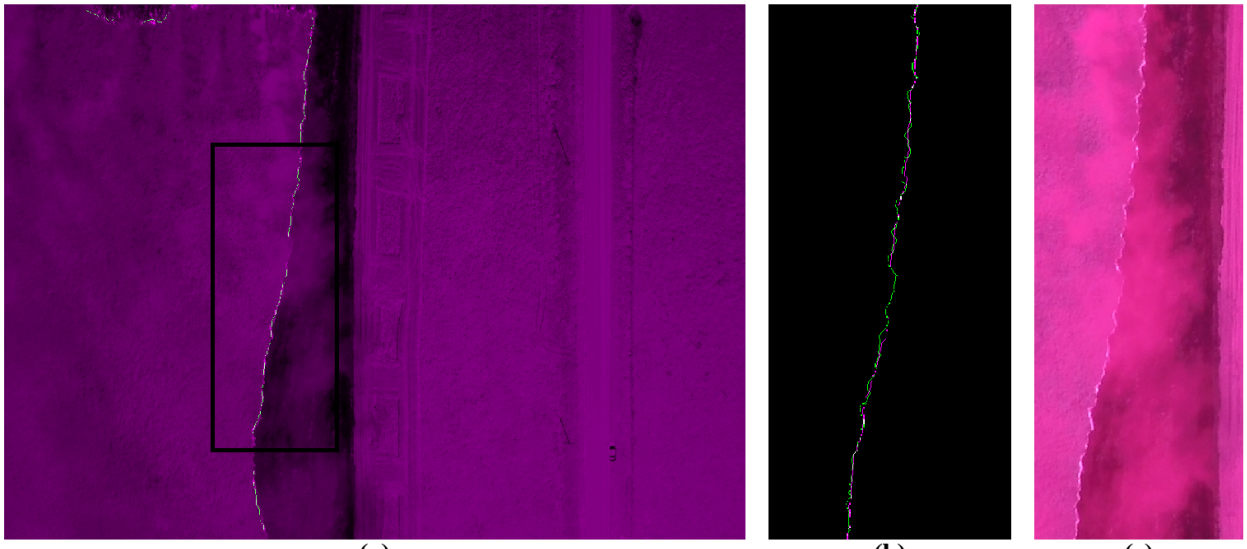

Figure 3.8: High Pratt Figure of Merit scored (PFOM = 0.738) cropped RGNIR image [a] with expanded fire region [c], algorithm estimate (purple), and manually labeled (green) fire fronts [b].

Figure 3.9 represents a typical image that produced a low merit score and contains two main issues within the algorithm. First, the relative presence of active fire within the image is minimal, therefore the assumed standard deviation of the NIR channel is lower than expected and Eqn. 3.14 will allow areas of high reflectance to be candidate fire pixels. The RGNIR image candidate fire pixels before the dark region detection is shown in Figure 3.10. Besides the brighter sections of the grass field outside the fire area, the sun's reflection off the vehicle shown to the right of the active fire is also considered a fire pixel. Since the vehicle is close to the fire, and therefore the burnt region, that pixel after the dark region detection process is still considered part of the fire front.

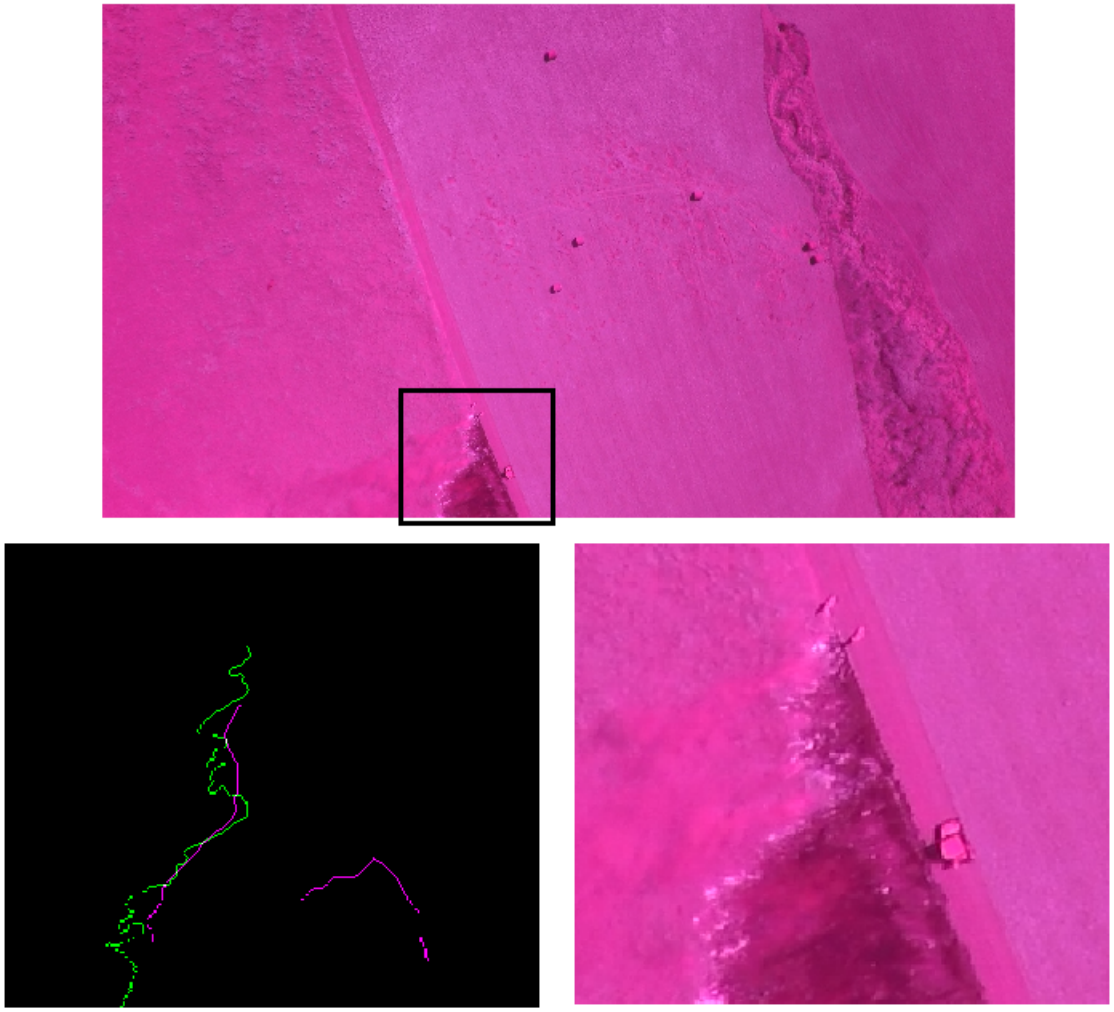

Figure 3.9: Low Pratt Figure of Merit scored (PFOM = 0.242) RGNIR image [top] with expanded fire region [bottom right], algorithm generated (purple), and manually labeled (green) fire fronts [bottom left].

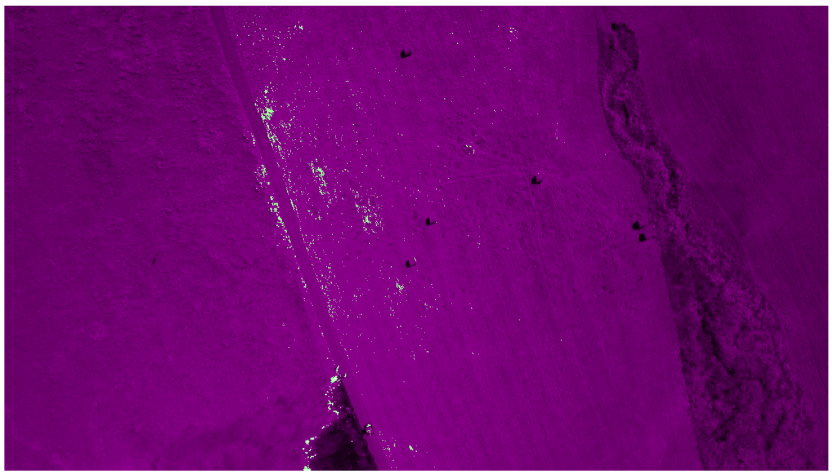

Figure 3.10: Low Pratt Figure of Merit score RGNIR image (Fig. 3.9) with detected fire pixels (green) before the dark region detection process.

When determining why an image produced a low or high PFOM score, two factors are evident from the PFOM equation itself (Eqn. 3.19) and are the primary variables when determining if a fire front was accurately portrayed: the cardinality difference and distance between the estimated and the ground truth fire front line. These factors convey if the correct amount of fire pixels were detected and how far the estimated lines were from the ground truth. To assist in quantifying cardinality differences, Eqn. 3.20 is used. Referred to as the Cardinality Difference Ratio (CDR), Eqn. 3.20 represents the absolute error of the cardinality between the ground truth and the algorithm fire front representations with respect to the cardinality of the ground truth line. Absolute error alone is not enough for error evaluation as images with low cardinality can still produce an incorrect fire front representation. An ideal algorithm estimate would produce a CDR of zero.

$$CDR = \frac{\left|card(I_{alg}) - card(I_{gt})\right|}{card(I_{gt})} \tag{3.20}$$

To observe the distance error between the algorithm estimate and the ground truth line, the root-mean square (RMS) Euclidean distance error is used. The CDR and RMS distance error for each image in the GRAFITTI dataset is shown in Figure 3.11 along with the image's respective PFOM score. The primary goal of the Pratt Figure of Merit is to quantify the two other parameters

shown in Figure 3.11 and to generate a single metric that represents the accuracy of edges within an image. However, when the goal is to grade a fire front line in the presence of false positives and minimal positional error around the manually labeled fire front, the PFOM score by itself is not enough by itself to determine success or failure.

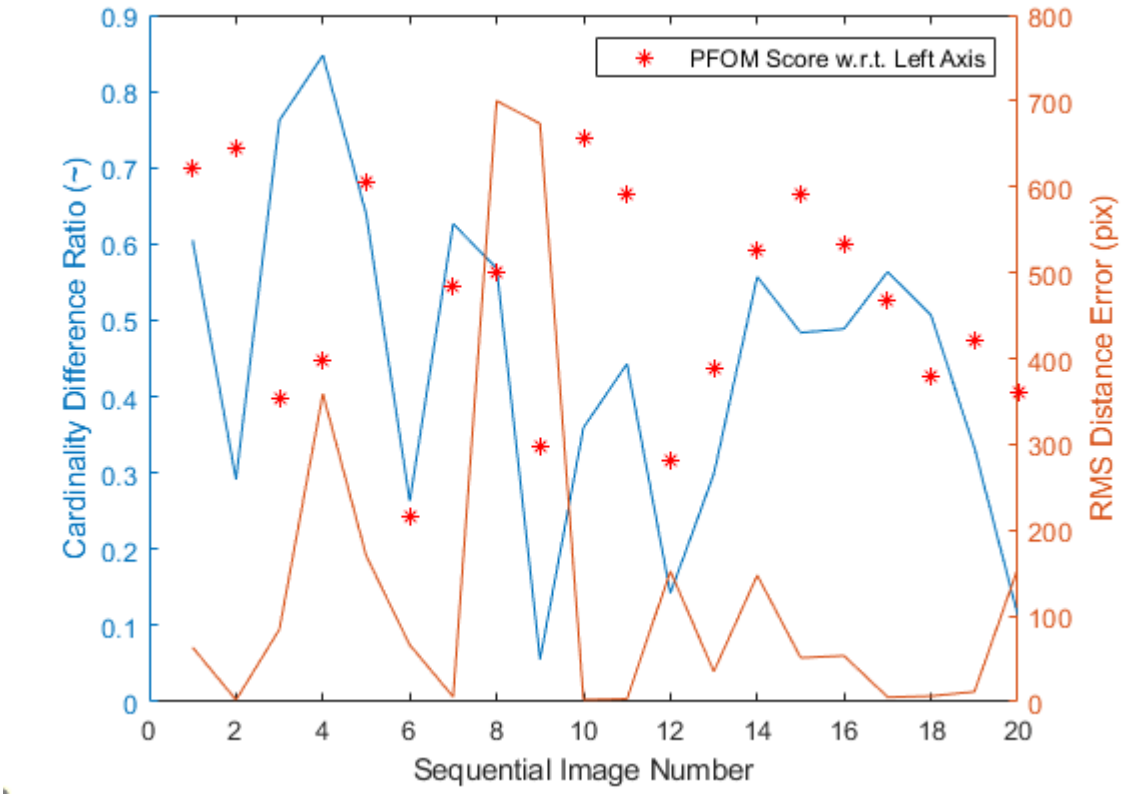

Figure 3.11: Cardinality Difference Ratio (CDR), RMS Distance Error and PFOM score.

An example case of successful identification using PFOM is shown in sequential images 8 and 9. Similar in environmental layout, 9 has a lower PFOM score even though it has a similar RMS error to 8 and a lower CDR value. Figure 3.12 presents pertinent sections of three images taken from the GRAFFITI dataset after processed in the NIR fire front identification algorithm, images 8, 9 and 18 sequentially. The respective values from Figure 3.12 are shown in Table 3.1. Images 8 and 9 present images taken roughly one second apart, yet according to Table 3.1 have vastly different PFOM scores and CDR values, but have similar RMS distance errors. While the fire fronts in both images are thin and difficult to detect in the NIR image due to lack of prominent fire areas,

both can distinguish the general shape and location of the fire line. Since both images contain a relatively small amount of fire pixels, reflective areas in the surrounding fields were also detected as fire, as shown in the right of the top and middle images of Figure 3.12. The primary difference between images 8 and 9 are the sparsely distributed false positive points in image 8 compared to the continuous, solid false front line seen in image 9 due to the dark region detector picking up sections of the darker brush not seen in image 8. While image 8 had a high cardinality difference when compared to image 9 (Table 3.1), the scarcity of false positives was not penalized as harshly in image eight's PFOM score. This is due to the false front line in image 9 being far from the ground truth line, thus the PFOM reflected that the large distance error was a higher penalty than overall cardinality.

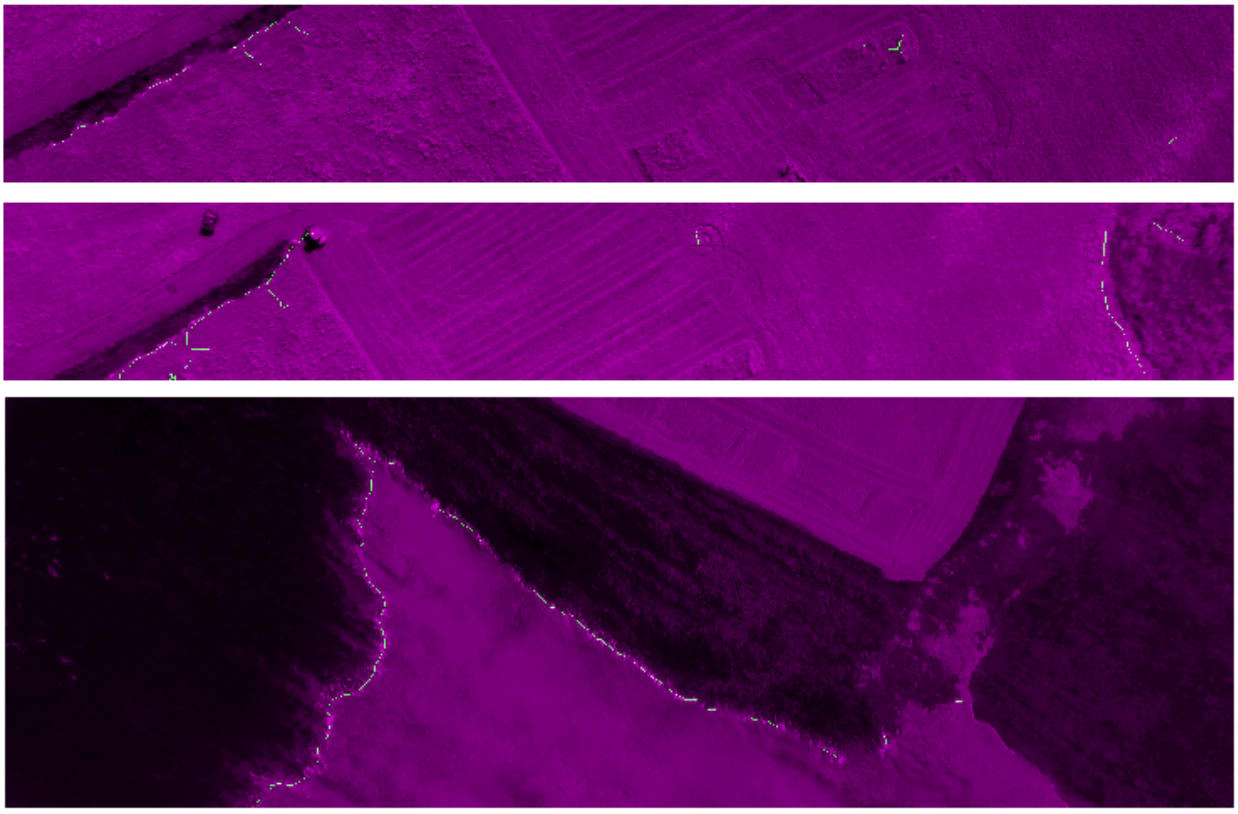

Figure 3.12: Cropped sections of images 8 (top), 9 (middle) and 18 (bottom) with identified fire front lines (green).

However, when comparing images 8 and 18 (top and bottom of Figure 3.12 respectively), where image 18 had no false positive fire pixels far from the fire front, the PFOM score was lower than

Table 3.1: Image analytics for Fig. 3.12.

Sequential Image #	PFOM Score $(\frac{1}{pix^3})$	CDR $(\sim)$	RMS Distance Error (pix)
8	0.545	0.568	700.13
9	0.334	0.056	673.46
18	0.426	0.507	6.76

expected when compared to image 8. From Table 3.1, images 8 and 18 share a similar CDR value, while the RMS distance error is greater in image 8 than in image 18. By observation, image 18 was able to accurately generate a fire front representation that portrays the shape and location of the imaged fire front, yet the PFOM of image 18 is over 0.1 and lower than image 8. The only major difference between the two images is the amount of fire present in the frame and therefore the cardinality of the ground truth fire front line is greater in image 18 than 8. When creating manual ground truth lines, minute details can be labeled where the algorithm is incapable of discerning. Figure 3.13 shows the algorithm produced line against the manually labeled fire front line. More fire pixels being present in the ground truth of image 18 than image 8. Along with the fact that the fire is thicker during the portion of the flight, the cardinality difference between the estimate and ground truth impacted the PFOM score of image 18 greater than the false positives in image 8 that are far away from the fire.

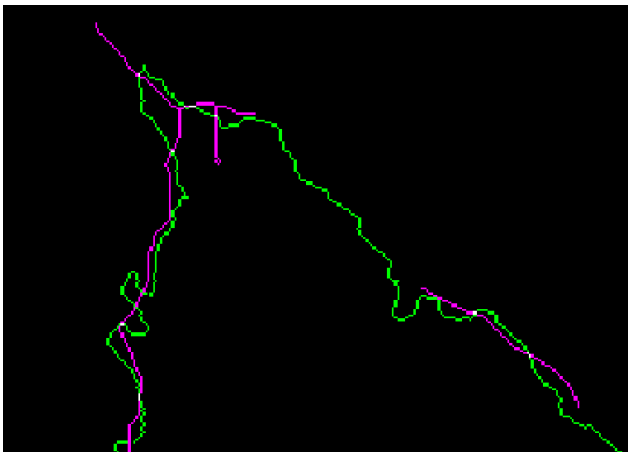

Figure 3.13: Image 18 ground truth (green) and algorithm produced (purple) fire front lines.

The PFOM score when applied to fire front identification based on a manually labeled fire front

line is vague as a standalone value, but generally produces a relative value between images. Compared to fire front and fire detection literature, most authors determine the problem of quantifying fire perimeter delineation as a segmentation task [10, 26, 38]. Remote sensing literature are more involved in the by-products of fire perimeter identification such as rate of spread (ROS) and use manual identification of fire fronts for continual work, but that process can be time consuming and has biases depending on the resolution and the fire environment [2, 39]. Automatic fire front detection has been accomplished and discussed before on an sUAS scale [40], but usually through the use of thresholds which need to be changed per image environment. Also, the results are rarely quantified against a ground truth image. While PFOM needs context regarding cardinality and distance error to identified fire fronts, it is a step towards validating fire front detection algorithms that can lead to real-time fire detection for fire fighting missions.

3.6 Conclusions

In this chapter, a new rule-based NIR fire identification algorithm was proposed for the problem of fire front detection in the NIR spectrum. The algorithm was validated using the 20 level 1 RGNIR images from the GRAFFITI dataset. After morphological processing, the algorithm produced a fire front line with an average Pratt Figure of Merit value of 0.523 over the dataset, which shows the effectiveness of the algorithm. Other observations show the ground truth cardinality difference played a role in the score of the algorithm, as the RMS distance error per fire pixel detected over the tested images was 1.02 pixels, or roughly 10 cm. For future work, a larger dataset will be tested. A new metric will be studied where a single value can accurately depict the success of fire line detection, independent of amount of fire pixels in an image. Additionally, real-time detection will be tested where the sUAS can follow and track the fire front.

Chapter 4

Grass Fire Front and Depth Estimation using NIR versus Thermal Images from sUAS: a Comparative Study

4.1 Introduction

This chapter focuses on a comparative study between the NIR image-based and thermal image-based fire metric estimation using the GRAFFITI dataset. Two grass fire metrics are the primary focus: fire front location and flame depth. Accurate measurement of the spread and shape of wildland grass fires is critical to fire behavior modeling, controlled burn planning and wildfire prevention. Fire metrics like rate of spread (ROS), flame depth, flame height and fire front location are critical to fire modeling and fire hazard prediction, but are difficult to measure in field settings on the ground [41]. Fire metrics have been measured in laboratory settings [42, 43], but are of particular interest in real prescribed fire and wildfire scenarios.

Many researchers have used satellite and airborne imagery to determine fire metrics such as the ROS and fire front location during wildfires. For example, satellite imagery has been used for active fire detection, damage assessment and fire spread modeling [39, 44–46] but has low spatial resolution and the time for observation can be longer than the duration of some wildfires last. Airborne images from manned aircraft have been used to find forest fire perimeter and active fire line that were used to develop fire propagation models [47]. Infrared imagery from aircraft have also been used to gathered measurements of heat and carbon fluxes, fire line geometry, and flame intensity [48]. Manned aircraft have been proven as a remote sensing platform to support fire mapping and metrics measurement, but are limited by pilot safety and operation costs.

sUAS have been used for wildfire remote sensing applications such as fire detection, damage assessment, vegetation density and progression monitoring [26, 49, 50]. A majority of these applications use thermal, near-infrared (NIR), or visual spectral cameras which have quite different spectral responses to fires in frame. The use of sUAS for fire metric measurement are limited in existing literature. Thermal and NIR images from a multi-rotor sUAS collected over prescribed fires in Montana and Oregon were used for fire ROS estimation [7]. Georeferenced orthomosaics from thermal images taken from the fixed-wing KHawk-55T were used for fire ROS measurement over a tall grass controlled burn with the field size of 650 m $\times$ 320 m [2]. Thermal or IR cameras are typically used over visible spectrum solutions as thermal images can see hot spots through smoke, where visible solutions have difficulties with occlusion [26]. Thermal cameras may pick up regions that are smoldering or no longer part of the flaming zone of a fire [51]. However, thermal imaging may suffer from pixel saturation over high temperature areas. Additionally, thermal reflections and heat radiation can create fire analogues within the thermal spectrum [8]. Visual and NIR solutions however can pick up light from flaming regions, which is an advantage over thermal imaging when determining a fire front or flame depth.

This chapter provides a comparative study for fire front location and flame depth estimation using RGNIR and thermal imagery taken by a sUAS with a nadir view. These spectra depict the fire front differently, and therefore may introduce different challenges in analysis including illumination, occlusion, and saturation issues. The objective is to quantify which method is more accurate in determining the fire front and flame depth of the observed fire. The obtained results can be used to guide future researchers in instrument selection for fire front delineation and fire behavior characterization.

This chapter is organized as the following, the fire front detection basics of NIR and thermal imagery are described in Section 4.2. Representative images from the GRAFFITI dataset are then used for the comparative evaluation of both methods for fire front and depth estimation in Section 4.3. Conclusions and directions for future work are discussed in Section 4.4.

4.2 NIR and Thermal Fire Front Signatures

Electro-optical sensors are the primary method for observation and measurement of wildland fires. Different sensors can detect the various indicators of fire: heat, light, smoke, flicker, motion and chemical byproducts [8]. The two sensors for discussion in this section are the thermal and visual/NIR-band cameras used to generate the GRAFFITI dataset 2. Each camera can detect the presence of fire, but the representation of the fire perimeter differs. Thermal cameras do not detect photons like visual-band cameras, but react to temperature changes of a detection material. A thermal image will depict the absorbed radiation in the camera sensor material caused by heat emitted during the fire.

Thermal images are typically chosen for mitigating smoke occlusion, which is the primary difficulty when observing fire using visual-band cameras [52]. Additionally, thermal cameras are used for environmental monitoring during the night and day, while visual cameras can only be used in daylight conditions. The peak radiance for fire is in the range of 8 - 12 μm, which is within the designed range of the thermal camera used in the GRAFFITI dataset (Table 2.1). However, in observation of open flame or smoldering fires, radiance response peaks at shorter wavelengths (3 - 5 μm) [8]. From a nadir perspective, the flame and smoldering fire base become difficult to distinguish as the flame is a lower temperature than the ground. Especially in high temperature situations, thermal imaging at high resolutions can become saturated. An extremely small and hot fire spot can appear larger in the thermal response due to the area dominating the temperature response of the fire area. Detecting fire in thermal images is nontrivial as thermal reflections, outside heat radiation, and infrared blocking can occur in thermal cameras to create fire analogues [51].

Visual/NIR-band camera solutions are used in fire detection but are limited historically for missed fire detection and high false positive rates. These systems are also sensitive to environmental conditions and illumination differences between different sets of fire images. However, visible solutions work based on light reflections; since flames are a light source, visual/NIR-band solutions can pick up smoldering fire and flames at wavelengths less than 3 μm [8]. Visual/NIR-band

cameras can usually aquire images at high frame rates (29.97 Hz) with higher resolution image sensors than thermal cameras at a fraction of the cost. While unable to achieve full fire awareness like a thermal camera, the unsaturated fire pixels found in visual/NIR-based cameras provide an alternative approach to determine the fire front location at a much higher spatial resolution.

The difference in the fire front observation from the thermal and NIR bands can be found in Fig. 4.1, which presents the image pair 11 in GRAFFITI dataset. The images show the Southwest portion of the prescribed fire which include the head fire (South fire front) and flank fire (West fire front). Fig. 4.1b is a histogram adjustment of the raw thermal image (4.1a) for better visualization of the surrounding features. The adjusted thermal image also shows the saturation effect of high temperature areas that are not flaming at this point during the controlled burn. The saturation effect along the head fire front is more prominent than the flank fire.

When comparing both thermal images to the RGNIR image (Fig. 4.1), two characteristics are evident: smoke occlusion and flame observation. The smoke from the head fire covers the flank fire along the West side of the fire perimeter, occluding the thin fire line and diminishing the strong emitted fire light from under the smoke. Additionally, the depth of the fire appears thinner in the RGNIR spectrum than in the thermal images.

The reft-most white region of the fire field in Fig. 4.1a and 4.1b is imperceptible in the RGNIR image. This section of the fire is no longer combusting, yet the residual hot ground beneath the extinguished flame is detected as part of the fire perimeter in the thermal spectrum. However, the RGNIR image presents a discontinuous fire front from smoke occlusion and the thin nature of the fire. Fig. 4.2 presents an overlay of the RGNIR image with a binary fire pixel mask from the thermal image; a thermal pixel is determined to be fire if the digital number is above 90% of the maximum intensity pixel within the thermal image [53]. As shown, the high intensity pixels of the RGNIR image along the head fire are not continuous due to smoke occlusion and flame flicker effects. While the image only has a reprojection error of less than 2 pixels, the thermal image fire front is off significantly along the head fire and within error on the flank side. The limitations between the two spectral images are supported by observations in other datasets.

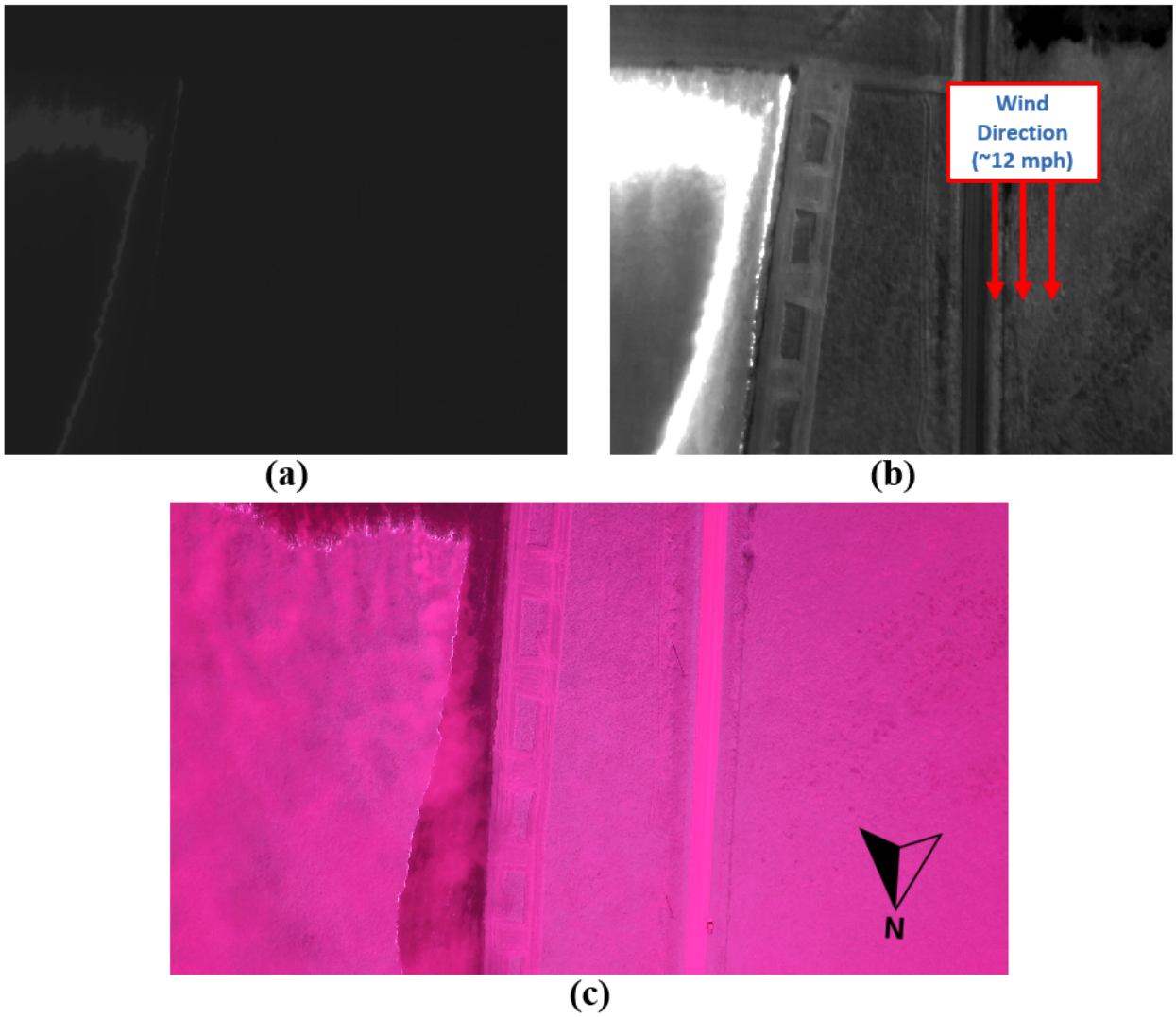

Figure 4.1: Image 11 of GRAFFITI dataset with primary wind direction: raw thermal image (a), histogram adjusted thermal image (b), and paired RGNIR image (c).

4.3 Fire Metrics Measurement Comparison

Flame dimension measurement is critical to fire modeling research as the rate of energy released by a spreading fire is directly correlated to the flame depth and ROS. Accurate quantification of these dimensions can lead to a better understanding of the fire impact, suppression requirements and size of the safety zone around a wildland fire [54]. Before analyzing the dimensional accuracy between the thermal and RGNIR images, the fire front and back must be delineated. Determining the fire front on thermal and NIR imagery has previously been performed using edge detection

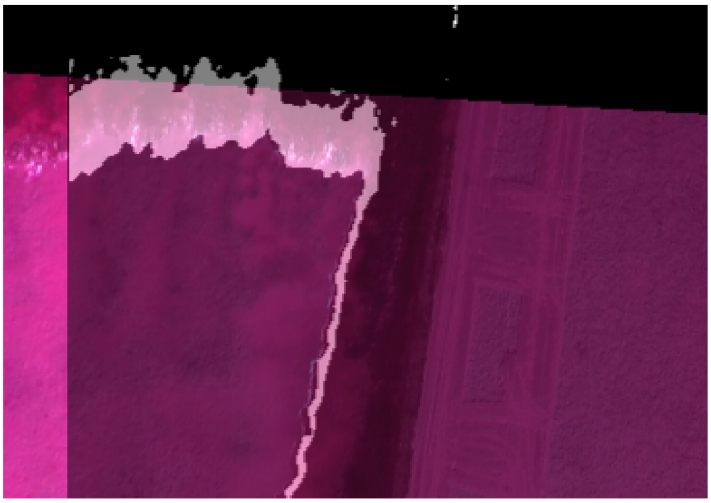

Figure 4.2: Cropped RGNIR image and detected thermal fire pixel overlay of GRAFFITI dataset: image 11.

algorithms such as Canny edge detection and Laplacians [39]. Similar methods have been used on NDVI imagery, derived from the NIR spectrum, using the zero-crossing of the derivative image to define the fire perimeter.

The NIR detection algorithm from Ch. 3 is used for the determiniation of the fire front location and flame depth. The thermal image fire pixels are determined using methodology from [2, 53], where any pixels above 90% of the maximum intensity pixel in an image is considered part of the fire perimeter. Two image pairs from the GRAFFITI dataset with less than 2 pixels RMS reprojection error will be used for analysis. It is assumed that the images are perfect nadir views since the caera orientation angles are small (<15 deg.). Fig. 4.3 shows the raw RGNIR and histogram adjusted thermal images for the two image pairs used for flame dimension comparison: image 11 and 20 of the GRAFFITI dataset. Fig. 4.4 shows the overlays between the fire pixels found using the NIR algorithm (purple) in Ch. 3 and the thermal fire detection (green) described above.

4.3.1 Fire Front Detection Comparison

To represent the fire front in the RGNIR and thermal images, an inset profile line similar to [39] is used. Inset maps were used to observe fire front delineations of a thermal image against the

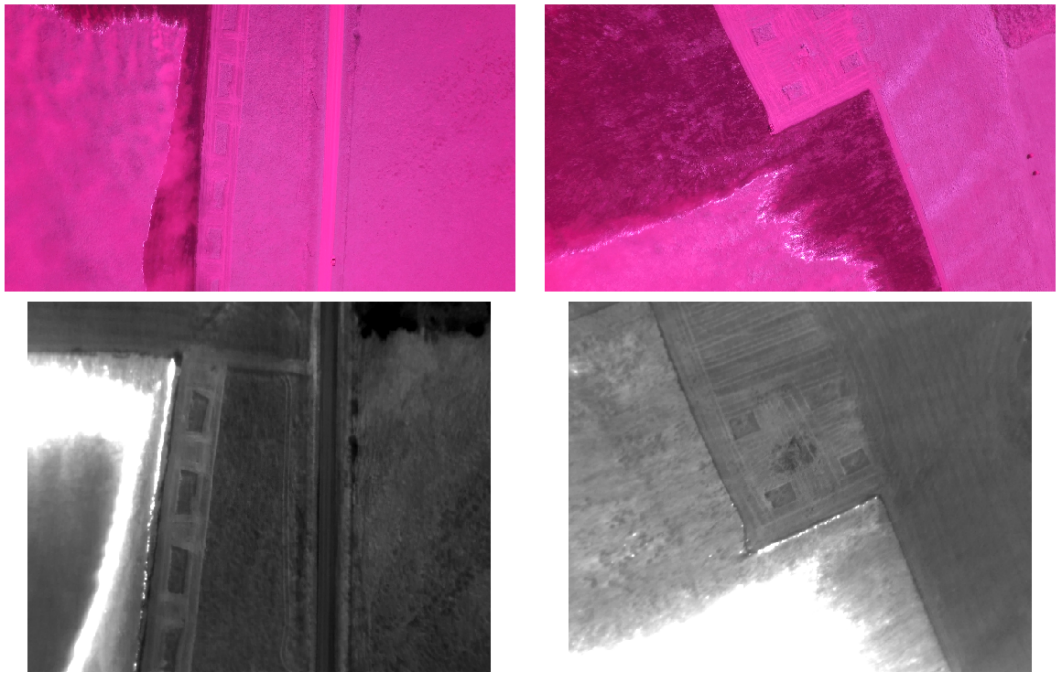

(a) (b)

Figure 4.3: Raw RGNIR and adjusted thermal image pairs for image 11 (a) and 20 (b) of GRAFFITI dataset.

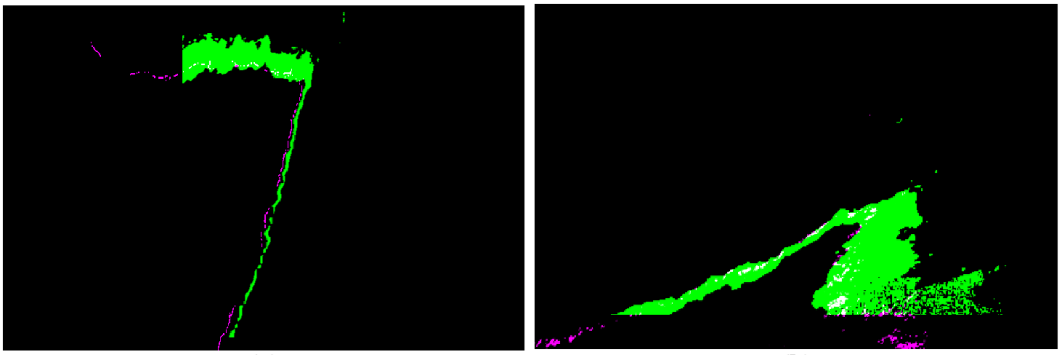

(a) (b)

Figure 4.4: Cropped overlays of RGNIR (purple) and thermal (green) fire pixels of image 11 (a) and 20 (b) from GRAFFITI dataset.

temperature gradient along the inset line [39]. For this section, Fig. 4.5 presents the inset profile lines used for fire front detection. The origin point for each line, represented by a red dot in Fig. 4.5, is within the unburned area inside the fire perimeter. All four profile lines then extend over the fire front line and past the fire backline. The directions of the inset profile lines were defined to be perpendicular (flank fires) or parallel (heading fires) based on the mean wind direction.

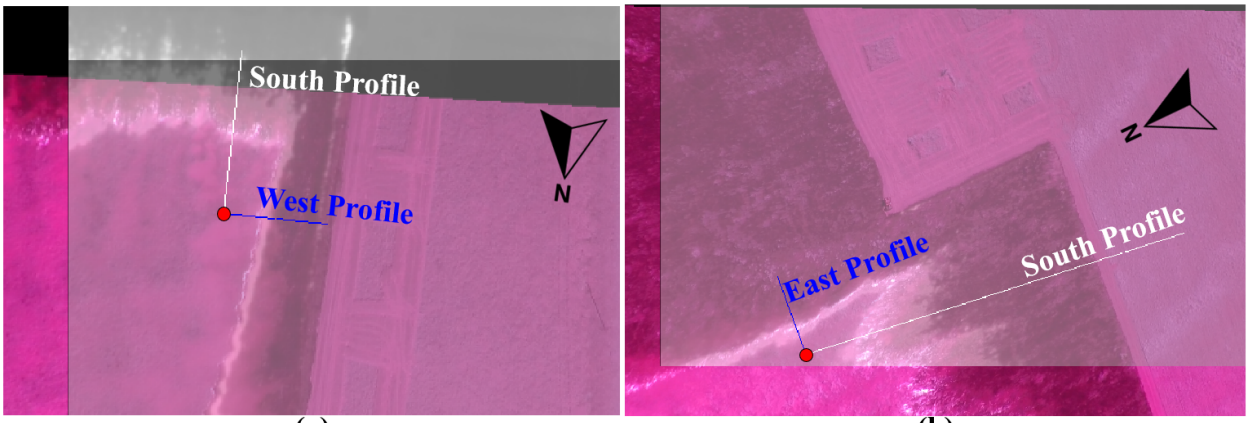

Figure 4.5: Inset profile line definitions for fire front detection in image 11 (a) and image 20 (b) of the GRAFFITI dataset.

The results on detected fire front and back lines along the inset lines are shown in Fig. 4.6. Along with the intensity response in the thermal and RGNIR channels, the solid gray areas shows the depth of the fire in the thermal image while the dashed black lines show where fire pixels were detected using the NIR algorithm. The southern line shows the thermal image fire front is about a meter in front of the RGNIR front, while the western line shows the algorithm estimated front is less than half a meter ahead of the thermal fire front.

Image 11 has a reprojection error of roughly two pixels and a spatial resolution of 0.23 $^{m}/_{pix}$. Therefore, the difference between the delineated fire fronts in the west line are within error and depict the fire front at the same location. The southern fire front difference of one meter is larger than the location error, demonstrating an offset when observing head fire front in the two spectrums. The thermal fire front seems to extend from the flame front observed in the RGNIR image. This is primarily due to radiant heat being carried by the smoke. Although hot spots can be detected by thermal images through smoke, the high temperature of the smoke occludes the true position of the fire front. At low resolutions the positional difference is negligible, but for the low altitude and high-resolution thermal images of the GRAFFITI dataset, the smoke clearly carries the apparent fire front ahead of the flaming front.

The results of the inset lines from image 20 show a similar trend (Fig. 4.7). The thermal and RGNIR images were taken at a later time than image 11, allowing the fire front to evolve. The

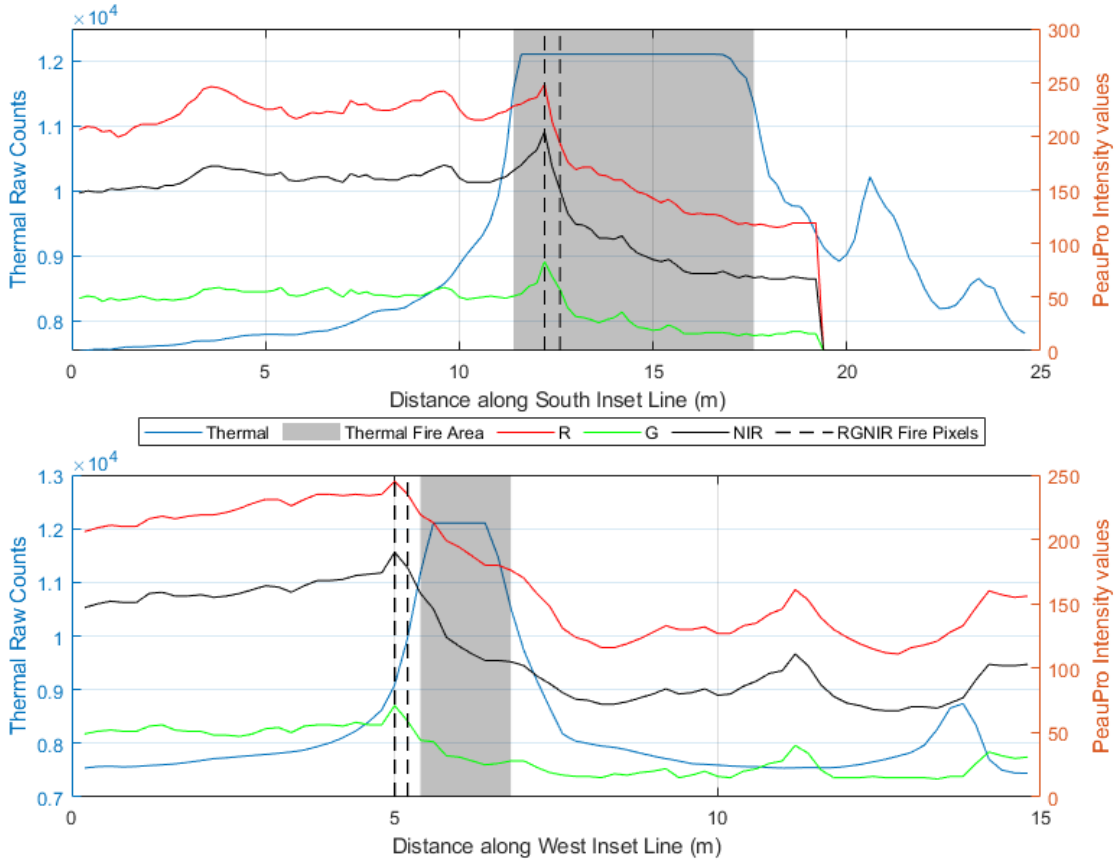

Figure 4.6: Inset profile line results for image 11 (4.5a) with marked fire positions in the thermal and RGNIR image.

difference between the southern fire fronts is 1.4 m where the algorithm estimated fire front is behind the thermal front. This can again be contributed to the smoke leading the head fire front in the thermal image; where the heat of the fire produces high temperature smoke and moves the apparent fire front forward. Conversely to the results of the flank fire front in Fig. 4.6, the thermal front is leading the RGNIR fire front by 1.6 m. The reprojection error of image 20 is slightly over a pixel, therefore the positional difference is not contributed to image misalignment.

Further observation of Fig. 4.3 shows the wind and smoke direction are not directly to the North, but due slightly Northwest. This would cause smoke from the East flank to move slightly forward of the spread direction and slightly behind the spread direction the West flank fire front. Smoke along the Western front does not affect the fire front detection as the high temperature

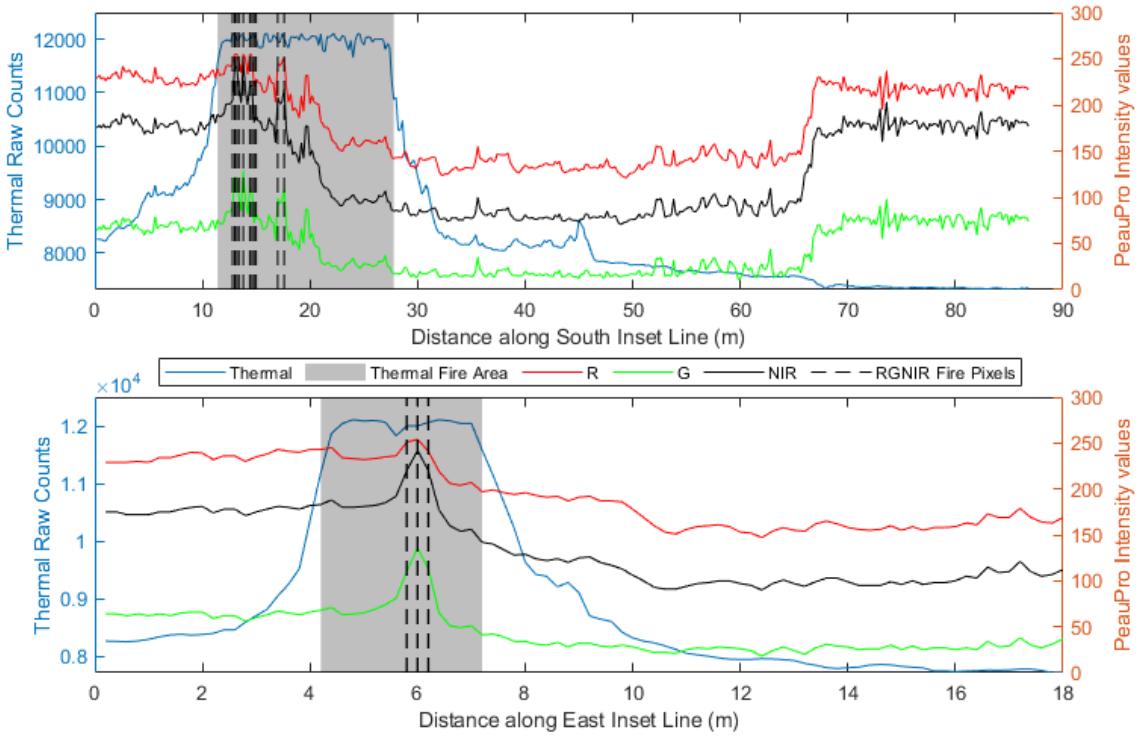

Figure 4.7: Inset profile line results for image 20 (4.5b) with marked fire positions in the thermal and RGNIR image.

smoke is carried back over the fire, allows the thermal camera to still get a clear view of the flaming front. However, the Eastern fire front in the thermal image will be pulled ahead of the flaming front due to the smoke from the prescribe fire. The difference between the smoke and wind direction against the Eastern and Western fire flanks once again shows that in the thermal image, smoke can slightly obfuscate the apparent fire front compared to the visual/NIR-based camera solution.

4.3.2 Flame Depth Estimation Comparison

Flame depth is defined as the width of the area where continuous flaming combustion occurs behind the leading edge of the fire front [54]. Historical determination of the trailing edge of the flaming zone has been considered subjective and difficult to locate due to the transient state between the flaming and smoldering combustion of the flame back [55]. For initial analysis of the flame zone depth of the images in Fig. 4.3, a similar approach is taken from the previous section. An inset

profile can observe the first and last instance of detected fire along the line and the distance between the two can determine the flame depth along the line. By measuring the detected fire locations across multiple inset lines along the fire perimeter, the fire depth can be calculated.

Fig. 4.8 presents the four regions used for initial analysis of the flame depth of the prescribed fire used in the GRAFFITI dataset. The green lines are the edges of the detected fire pixels in the thermal image, using the 90% maximum intensity threshold. The purple pixels are a combination of the detected fire pixels and the fire front representation using the NIR algorithm described in Ch. 3. The four regions used for flame depth calculation are shown in yellow. The red line indicates the position of the first inset profile line and the region ends at the blue inset profile line shown in Fig. 4.8.

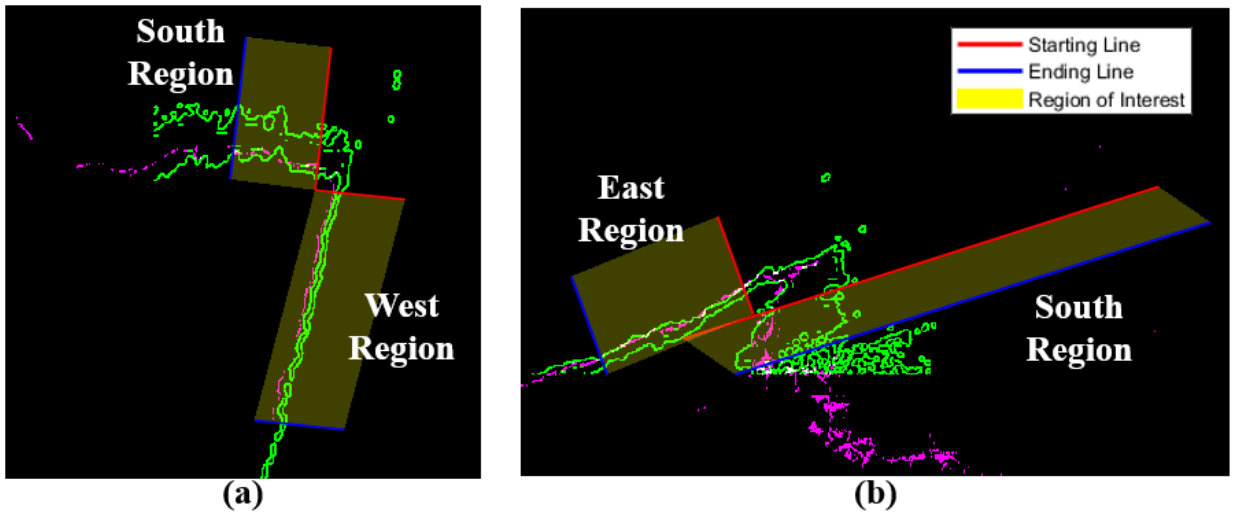

Figure 4.8: Flame depth evaluation regions in image 11 (a) and image 20 (b) of the GRAFFITI dataset.

Fig. 4.9 shows the results for the flame zone depth along the selected inset lines in the South and West regions. The NIR detection algorithm occasionally found no points along the inset profile, and those are excluded from the flame depth figures. For the South and West sections of the fire perimeter, the average flame depth using NIR detection was 0.74 m and 0.25 m, respectively. This reflects the relation between head and flank fires as the prevailing wind creates a thicker flame when compared to the apparently thin flames of the flank fire [41]. On the other hand, the flame

depth derived from the thermal fire detection is much larger and not reliable due to the fire pixel saturation issue and the transient nature of combustion at the fire back line. While the flame is not present, the burnt grass and ground below are still hot from the passing fire. Similar to how smoke can create a flame analogue in thermal fire front detection, residual heat behind the flame zone has high thermal emissivity [39]. This thermal interaction causes the apparent back of the fire perimeter to be further behind the fire than other sensors would detect.

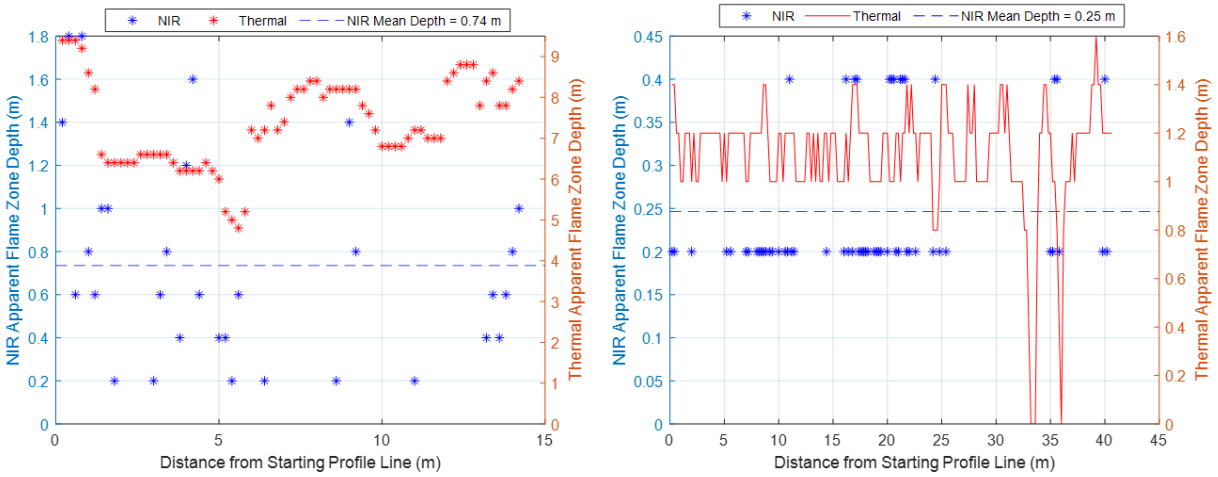

(a) **(b)**

Figure 4.9: Flame zone depth for South (a) and West (b) regions of image 11.

Fig. 4.10 shows a similar relationship between the thermal and NIR algorithm detected flame depths. With the average head flame depth at 2.85 m and the flank depth at 0.37 m, both values show the head fire is thicker as the fire evolves and the flank depth remains relatively steady when compare to the values from image 11 (Fig. 4.9). The average and standard deviation (STD) for flame depth of the four fire regions described are shown in Table 4.1.

Table 4.1: Flame depth statistics from NIR GRAFFITI images.

Image # & Position	NIR mean (μ_{NIR}) [m]	NIR STD (σ_{NIR}) [m]
Img. 11 West	0.25	0.09
Img. 11 South	0.74	0.47
Img. 20 East	0.37	0.18
Img. 20 South	2.85	1.24

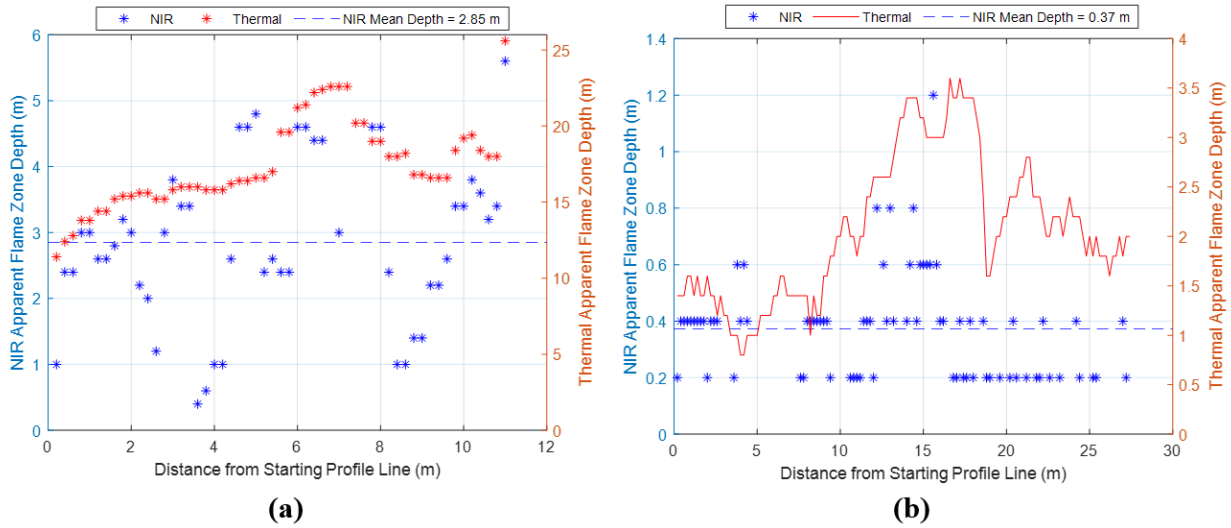

Figure 4.10: Flame zone depth for South (a) and East (b) regions of image 20.

Flame-front residence time is used for quantifying which result is more accurate. Residence time (τ_r) is the length of time for a flame zone to pass over a given point. It is an important characteristic for describing a wildfire as it represents the convective heating above a surface fire [55, 56]. The definition for flame-front residence time is given below:

$$\tau_r = \frac{D}{ROS} \tag{4.1}$$

where D is the flame depth and ROS is the rate of spread. Residence time can be on the scale of minutes or seconds, primarily varying based on the fuel type and distribution [57]. For wildland grass fires like the prescribed burn in the GRAFFITI dataset, the estimated residence time is between 1 - 5 seconds for light pastures or 10 - 15 seconds in heavy pastures [41].

Rate of spread for the prescribed fire used in the GRAFFITI dataset has been previously calculated in the same sections of the fire field shown in Fig. 4.3 [2]. The results for residence time using the average fire depth found in the thermal and algorithm are shown in Table 4.2. The residence time found using the NIR algorithm closely matches the estimates for grass fires provided in [41].

Table 4.2: Flame depth statistics from GRAFFITI images.

Image # & Position	ROS (m/s) [2]	NIR depth mean (μ_{NIR})[m]	NIR residence time, $\tau_{r,NIR}$ (s)
Img. 11 West	0.08	0.25	3.13
Img. 11 South	0.22	0.74	3.36
Img. 20 East	0.11	0.37	3.36
Img. 20 South	0.28	2.85	10.18

4.3.3 Discussions & Suggestions

The overlay comparisons shown in sections 4.3.1 and 4.3.2 present the difference in observation between thermal and RGNIR bands over the same fire front. While thermal imagery is typically preferred for identification of fire hot spots through smoke, the radiant heat in smoke causes the detected fire front to be in front of head fires detected by the NIR-based method. When analyzing wildfires with a significant amount of smoke or rapidly changing wind conditions, measuring fire front location using only thermal imagery can potentially lead to small bias errors. Additionally, thermal images are not reliable for flame zone depth determination due to the ambiguous nature of temperature detection behind a fire front.

While visual/NIR-based solutions for observing wildland grass fires can create false positives, the accuracy of fire localization and measurement is better than thermal imagery if smoke obscuration is not significant. Both in-expensive and typically higher resolution than thermal cameras, visual/NIR-based multispectral cameras are shown to have some advantages when delineating fire metrics such as fire front location and flame zone depth with minimal to no smoke occlusion. Thermal cameras are recommended to be used for high altitude monitoring or thick smoke situations.

4.4 Conclusions

This chapter presented a comparative study on the differences between fire detection in thermal and NIR imagery. Thermal and NIR overlays from the GRAFFITI dataset of a head and flank fire showed that while the high temperature fire can be easily detected in thermal spectrum, saturation

and high temperature smoke can move the apparent fire front forward when compared to the detected front from the NIR algorithm. Additionally, the RGNIR images provided a flame depth of 0.25 - 2.85 m, within expected values from literature. This chapter provides the first quantification of thermal and vision-based fire metrics at the sUAS scale and provide situations of when to use each spectrum in wildland grass fire observation and measurement. Future work needs to be done regarding other spectrums including short-wave infrared or a typical RGB color band. Additionally, further fire metrics should be derived from nadir thermal and NIR imagery for use in fire prevention, modeling and real time detection like flame height, flame length and georeferenced position.

Chapter 5

Conclusions and Future Work

5.1 Conclusions

The GRAFFITI dataset, a new multispectral wildland grass fire dataset is created in this thesis using sUAS imagery. This dataset aims to address the challenges in low altitude fire observation and fire metrics measurement using thermal and NIR aerial imagery.

Chapter 2 described the acquisition and development of the 70 image GRAFFITI dataset. Current fire datasets include either imagery from oblique viewpoints or do not have a shared field of view over the fire burning scene from multiple spectral bands. The GRAFFITI level 1 dataset has 20 raw RGNIR and thermal image pairs of a grass fire. For level 2, the homograph for 15 image pairs were estimated with a low mean reprojection error of 1.26 pixels. The overlaid imagery allows for further comparison on fire metrics determination using the RGNIR and thermal bands.

In Chapter 3, a novel rule-based NIR fire detection and fire front identification algorithm was proposed. Using the 20 RGNIR images from level 1 of the GRAFFITI dataset, the average fire front line produced a Pratt Figure of Merit score of 0.523. The effectiveness of the algorithm is also shown by a small RMS distance error of 10 cm when comparing the detected fire front to the manually delineated ground truth.

Finally, Chapter 4 discussed and analyzed the differences in the fire front and flame depth estimation using thermal and NIR imagery. While thermal cameras could accurately detect the presence of fire, the radiant heat from smoke and the smoldering ground behind the fire front may affect fire metrics measurement. On the other side, while NIR based fire detection can lead to a discontinuous fire front, the fire front location and flame depth estimates are more accurate when

the effect of smoke is negligible. Initial fire depth estimation results showed the feasibility of NIR imagery through the GRAFFITI dataset.

5.2 Future Work

Several potential future directions can be explored from each of the three main focuses of the thesis:

1. Collection and creation of an improved multi-camera, multispectral dataset over wildland fires:
    - Improved hard-mounted payload bays for consistent camera alignment;
    - Automatic feature matching between different bands which require feature identifiers that are independent of the image spectrum.
2. NIR fire detection and fire front identification:
    - Use a larger dataset with different illumination and environments to verify the robustness of the NIR algorithm;
    - Define new metrics to compare fire front delineations based on positional accuracy over cardinality differences;
    - Apply to real-time fire detection systems which can track and develop live-mapping of a fire front.
3. Fire behavior metric analysis in thermal and NIR imagery:
    - Analyze additional fire metrics;
    - Include other spectra such as short-wave infrared spectrum and the RGB band.

References

[1] P. Productions. Peaupro60 NDVI 5.4mm (30mm) f/2.5 gopro hero 4 black. [Online]. Available: https://www.peauproductions.com/products/peaupro60-ndvi

[2] S. Gowravaram, H. Chao, T. Zhao, S. Parsons, X. Hu, M. Xin, H. Flanagan, and P. Tian, "Prescribed grass fire evolution mapping and rate of spread measurement using orthorectified thermal imagery from a fixed-wing UAS," *International Journal of Remote Sensing*, pp. 1–20, 2022.

[3] L. Wang, J. Qu, and X. Hao, "Forest fire detection using the normalized multi-band drought index (NMDI) with satellite measurements," *Agricultural and Forest Meteorology*, vol. 148, no. 11, pp. 1767–1776, 2008.

[4] K. Nakau, M. Fukuda, K. Kushida, H. Hayasaka, K. Kimura, and H. Tani, "Forest fire detection based on MODIS satellite imagery, and comparison of NOAA satellite imagery with fire fighters' information," in *IARC/JAXA Terrestrial Team Workshop*, 2006, pp. 18–23.

[5] J. D. Burnett and M. G. Wing, "A low-cost near-infrared digital camera for fire detection and monitoring," *International Journal of Remote Sensing*, vol. 39, no. 3, pp. 741–753, 2018.

[6] T. Toulouse, L. Rossi, A. Campana, T. Celik, and M. A. Akhloufi, "Computer vision for wildfire research: An evolving image dataset for processing and analysis," *Fire Safety Journal*, vol. 92, pp. 188–194, 2017.

[7] C. J. Moran, C. A. Seielstad, M. R. Cunningham, V. Hoff, R. A. Parsons, L. Queen, K. Sauerbrey, and T. Wallace, "Deriving fire behavior metrics from UAS imagery," *Fire*, vol. 2, no. 2, p. 36, 2019.

[8] R. S. Allison, J. M. Johnston, G. Craig, and S. Jennings, "Airborne optical and thermal remote sensing for wildfire detection and monitoring," *Sensors*, vol. 16, no. 8, p. 1310, 2016.

[9] M. J. Sousa, A. Moutinho, and M. Almeida, "Thermal infrared sensing for near real-time data-driven fire detection and monitoring systems," *Sensors*, vol. 20, no. 23, p. 6803, 2020.

[10] J. Doshi, D. Garcia, C. Massey, P. Llueca, N. Borensztein, M. Baird, M. Cook, and D. Raj, "Firenet: Real-time segmentation of fire perimeter from aerial video," *Conference on Neural Information Processing Systems*, 2019.

[11] R. E. Burgan, *Using NDVI to assess departure from average greenness and its relation to fire business*. US Department of Agriculture, Forest Service, Intermountain Research Station, 1996, vol. 333.

[12] A. Shamsoshoara, F. Afghah, A. Razi, L. Zheng, P. Z. Fulé, and E. Blasch, "Aerial imagery pile burn detection using deep learning: The FLAME dataset," *Computer Networks*, vol. 193, p. 108001, 2021.

[13] Getfpv.com. Zii zephyr 2 wing. [Online]. Available: https://www.getfpv.com/zii-zephyr-2-wing.html

[14] *U-blox M8 concurrent GNSS modules data sheet*, u-blox, 10 2021, rev. 11.

[15] FLIR. Vue pro r specifications. [Online]. Available: https://www.flir.com/products/vue-pro-r/?vertical=suas&segment=oem

[16] Sep 2019. [Online]. Available: https://flir.custhelp.com/app/answers/detail/a_id/3134/~/adjusting-sensitivity-/%26-gain-on-the-flir-vue-pro-r

[17] L. H. Schinasi, T. Benmarhnia, and A. J. De Roos, "Modification of the association between high ambient temperature and health by urban microclimate indicators: A systematic review and meta-analysis," *Environmental Research*, vol. 161, pp. 168–180, 2018.

[18] R. Hartley and A. Zisserman, *Multiple View Geometry in Computer Vision*, 2nd ed. Cambridge University Press, 2004.

[19] J. Goyer, "Adaptive template matching (ATM) for vision-aided navigation," 2019.

[20] P. H. Torr and A. Zisserman, "MLESAC: A new robust estimator with application to estimating image geometry," *Computer Vision and Image Understanding*, vol. 78, no. 1, pp. 138–156, 2000.

[21] W. Phillips Iii, M. Shah, and N. da Vitoria Lobo, "Flame recognition in video," *Pattern Recognition Letters*, vol. 23, no. 1-3, pp. 319–327, 2002.

[22] T.-H. Chen, P.-H. Wu, and Y.-C. Chiou, "An early fire-detection method based on image processing," in *2004 International Conference on Image Processing, 2004. ICIP'04.*, vol. 3. IEEE, 2004, pp. 1707–1710.

[23] G. Marbach, M. Loepfe, and T. Brupbacher, "An image processing technique for fire detection in video images," *Fire safety journal*, vol. 41, no. 4, pp. 285–289, 2006.

[24] T. Celik and H. Demirel, "Fire detection in video sequences using a generic color model," *Fire Safety Journal*, vol. 44, no. 2, pp. 147–158, 2009.

[25] L. Rossi, M. Akhloufi, and Y. Tison, "On the use of stereovision to develop a novel instrumentation system to extract geometric fire fronts characteristics," *Fire Safety Journal*, vol. 46, no. 1-2, pp. 9–20, 2011.

[26] C. Yuan, Z. Liu, and Y. Zhang, "Fire detection using infrared images for UAV-based forest fire surveillance," in *2017 International Conference on Unmanned Aircraft Systems (ICUAS)*. IEEE, 2017, pp. 567–572.

[27] L. Merino, F. Caballero, J. R. Martínez-de Dios, I. Maza, and A. Ollero, "An unmanned aircraft system for automatic forest fire monitoring and measurement," *Journal of Intelligent & Robotic Systems*, vol. 65, no. 1, pp. 533–548, 2012.

[28] V. G. Ambrosia, S. Wegener, T. Zajkowski, D. Sullivan, S. Buechel, F. Enomoto, B. Lobitz, S. Johan, J. Brass, and E. Hinkley, "The ikhana unmanned airborne system (UAS) western states fire imaging missions: from concept to reality (2006–2010)," *Geocarto International*, vol. 26, no. 2, pp. 85–101, 2011.

[29] H. Segah, H. Tani, and T. Hirano, "Detection of fire impact and vegetation recovery over tropical peat swamp forest by satellite data and ground-based NDVI instrument," *International Journal of Remote Sensing*, vol. 31, no. 20, pp. 5297–5314, 2010.

[30] T. K. Remmel and A. H. Perera, "Fire mapping in a northern boreal forest: assessing AVHRR/NDVI methods of change detection," *Forest Ecology and Management*, vol. 152, no. 1-3, pp. 119–129, 2001.

[31] B. C. Ko, K.-H. Cheong, and J.-Y. Nam, "Fire detection based on vision sensor and support vector machines," *Fire Safety Journal*, vol. 44, no. 3, pp. 322–329, 2009.

[32] E. Rosten and T. Drummond, "Machine learning for high-speed corner detection," in *European Conference on Computer Vision*. Springer, 2006, pp. 430–443.

[33] R. C. Gonzalez and R. E. Woods, *Digital Image Processing*. Pearson, 2018.

[34] L. Lam, S.-W. Lee, and C. Y. Suen, "Thinning methodologies - a comprehensive survey," *IEEE Transactions on Pattern Analysis & Machine Intelligence*, vol. 14, no. 09, pp. 869–885, 1992.

[35] I. E. Abdou and W. K. Pratt, "Quantitative design and evaluation of enhancement/thresholding edge detectors," *Proceedings of the IEEE*, vol. 67, no. 5, pp. 753–763, 1979.

[36] S. Wesolkowski, M. Jernigan, and R. D. Dony, "Comparison of color image edge detectors in multiple color spaces," in *Proceedings 2000 International Conference on Image Processing (Cat. No. 00CH37101)*, vol. 2. IEEE, 2000, pp. 796–799.

[37] B. O. Sadiq, S. Sani, and S. Garba, "Edge detection: A collection of pixel based approach for colored images," *International Journal of Computer Applications*, vol. 113, no. 5, 2015.

[38] S. Sudhakar, V. Vijayakumar, C. S. Kumar, V. Priya, L. Ravi, and V. Subramaniyaswamy, "Unmanned aerial vehicle (UAV) based forest fire detection and monitoring for reducing false alarms in forest-fires," *Computer Communications*, vol. 149, pp. 1–16, 2020.

[39] D. Stow, P. Riggan, G. Schag, W. Brewer, R. Tissell, J. Coen, and E. Storey, "Assessing uncertainty and demonstrating potential for estimating fire rate of spread at landscape scales based on time sequential airborne thermal infrared imaging," *International Journal of Remote Sensing*, vol. 40, no. 13, pp. 4876–4897, 2019.

[40] C. Yuan, Z. Liu, and Y. Zhang, "UAV-based forest fire detection and tracking using image processing techniques," in *2015 International Conference on Unmanned Aircraft Systems (ICUAS)*. IEEE, 2015, pp. 639–643.

[41] P. Cheney and A. Sullivan, *Grassfires: Fuel, Weather and Fire Behaviour*. Csiro Publishing, 01 2008.

[42] A. J. Simard, R. W. Blank, and S. L. Hobrla, "Measuring and interpreting flame height in wildland fires," *Fire Technology*, vol. 25, no. 2, pp. 114–133, 1989.

[43] M. A. Finney, J. Forthofer, I. C. Grenfell, B. A. Adam, N. K. Akafuah, and K. Saito, "Fire and explosion-a study of flame spread in engineered cardboard fuel beds part i: Correlations and observations of flame spread," in *Progress in Scale Modeling, Volume II: Selections from the International Symposia on Scale Modeling, ISSM VI (2009) and ISSM VII (2013)*. Springer, 2014, p. 71.

[44] I. A. Csiszar, J. T. Morisette, and L. Giglio, "Validation of active fire detection from moderate-resolution satellite sensors: The MODIS example in Northern Eurasia," *IEEE Transactions on Geoscience and Remote Sensing*, vol. 44, no. 7, pp. 1757–1764, 2006.

[45] C. Quintano, A. Fernández-Manso, L. Calvo, and D. A. Roberts, "Vegetation and soil fire damage analysis based on species distribution modeling trained with multispectral satellite data," *Remote Sensing*, vol. 11, no. 15, p. 1832, 2019.

[46] K. R. Anderson, P. Englefield, J. Little, and G. Reuter, "An approach to operational forest fire growth predictions for Canada," *International Journal of Wildland Fire*, vol. 18, no. 8, pp. 893–905, 2009.

[47] A. E. Ononye, A. Vodacek, and E. Saber, "Automated extraction of fire line parameters from multispectral infrared images," *Remote Sensing of Environment*, vol. 108, no. 2, pp. 179–188, 2007.

[48] P. J. Riggan, R. G. Tissell, R. N. Lockwood, J. A. Brass, J. A. R. Pereira, H. S. Miranda, A. C. Miranda, T. Campos, and R. Higgins, "Remote measurement of energy and carbon flux from wildfires in Brazil," *Ecological Applications*, vol. 14, no. 3, pp. 855–872, 2004.

[49] S. Samiappan, L. Hathcock, G. Turnage, C. McCraine, J. Pitchford, and R. Moorhead, "Remote sensing of wildfire using a small unmanned aerial system: Post-fire mapping, vegetation recovery and damage analysis in Grand Bay, Mississippi/Alabama, USA," *Drones*, vol. 3, no. 2, p. 43, 2019.

[50] E. Beachly, C. Detweiler, S. Elbaum, D. Twidwell, and B. Duncan, "UAS-Rx interface for mission planning, fire tracking, fire ignition, and real-time updating," in *2017 IEEE International Symposium on Safety, Security and Rescue Robotics (SSRR)*. IEEE, 2017, pp. 67–74.

[51] A. E. Çetin, K. Dimitropoulos, B. Gouverneur, N. Grammalidis, O. Günay, Y. H. Habiboğlu, B. U. Töreyin, and S. Verstockt, "Video fire detection – review," *Digital Signal Processing*, vol. 23, no. 6, pp. 1827–1843, 2013.

[52] J. R. Martinez-de Dios, B. C. Arrue, A. Ollero, L. Merino, and F. Gómez-Rodríguez, "Computer vision techniques for forest fire perception," *Image and Vision Computing*, vol. 26, no. 4, pp. 550–562, 2008.

[53] S. Gowravaram, "Multispectral remote sensing and spatiotemporal mapping of the environment and natural disasters using small UAS," Ph.D. dissertation, University of Kansas, 2022.

[54] M. G. Cruz and M. E. Alexander, "Flame dimensions," *Encyclopedia of Wildfires and Wildland-Urban Interface (WUI) Fires*, pp. 468–472, 2020.

[55] M. E. Alexander, "Crown fire thresholds in exotic pine plantations of Australia." Ph.D. dissertation, Australian National University, 1998.

[56] M. Alexander and M. Cruz, "Modelling the effects of surface and crown fire behaviour on serotinous cone opening in jack pine and lodgepole pine forests," *International Journal of Wildland Fire*, vol. 21, no. 6, pp. 709–721, 2012.

[57] R. M. Nelson Jr, "Reaction times and burning rates for wind tunnel headfires," *International Journal of Wildland Fire*, vol. 12, no. 2, pp. 195–211, 2003.

Appendix A

GRAFFITI Dataset Information and Examples

The full GRAFFITI dataset can be found on the CUSL "Flight Log" website (https://cusl.ku.edu/). Below, Table A.1 provides time, position, attitude and level 2 information for each image in the GRAFFITI dataset. Fig. A.1 provides the first four images of the level 1 and 2 of the GRAFFITI dataset.

Table A.1: GRAFFITI Level I Statistics

Image No. (∼)	Time (CST)	UTM Easting (m) [15S]	UTM Northing (m) [15S]	Roll (deg)	Pitch (deg)	Yaw (deg)	Level II Composite
1	12:10:14	300375.8	4228474.2	-3.39	3.18	173.28	Y
2	12:10:15	300379.3	4228455.9	0.53	2.32	173.22	Y
3	12:10:22	300477.5	4228370.1	-16.91	3.42	97.47	Y
4	12:12:46	300923.8	4228517.5	5.01	7.31	243.93	Y
5	12:12:47	300902.5	4228519.7	0.13	9.07	247.63	N
6	12:13:40	300592.2	4228327.8	7.25	7.54	106.27	N
7	12:09:01	300415.1	4228414.8	2.31	6.76	228.42	Y
8	12:09:23	300815.3	4228400.3	6.83	9.15	116.92	Y
9	12:09:24	300839.3	4228398.4	0.6	6.96	120.51	Y
10	12:10:16	300384.2	4228436.7	0.18	2.32	175.22	Y
11	12:10:16	300386	4228428.6	-1.54	1.68	174.92	Y
12	12:10:36	300851.7	4228437.5	-15.03	5.92	67.25	Y
13	12:10:37	300866	4228448.2	-11.08	7.86	67.71	N
14	12:10:39	300916.6	4228492.3	-6.65	9.18	57.94	N
15	12:13:10	300422.9	4228539.6	0.79	9.95	246.97	N
16	12:13:11	300410.2	4228539.9	4.22	8.78	247.47	Y
17	12:14:35	300445.7	4228486.9	-1.01	6.19	240.89	N
18	12:14:36	300421.6	4228486.7	1.42	4.65	246.07	Y
19	12:17:18	300457	4228483.3	0.75	8.23	243.96	Y
20	12:17:47	300808.5	4228395.8	-1.94	4.66	111.79	Y

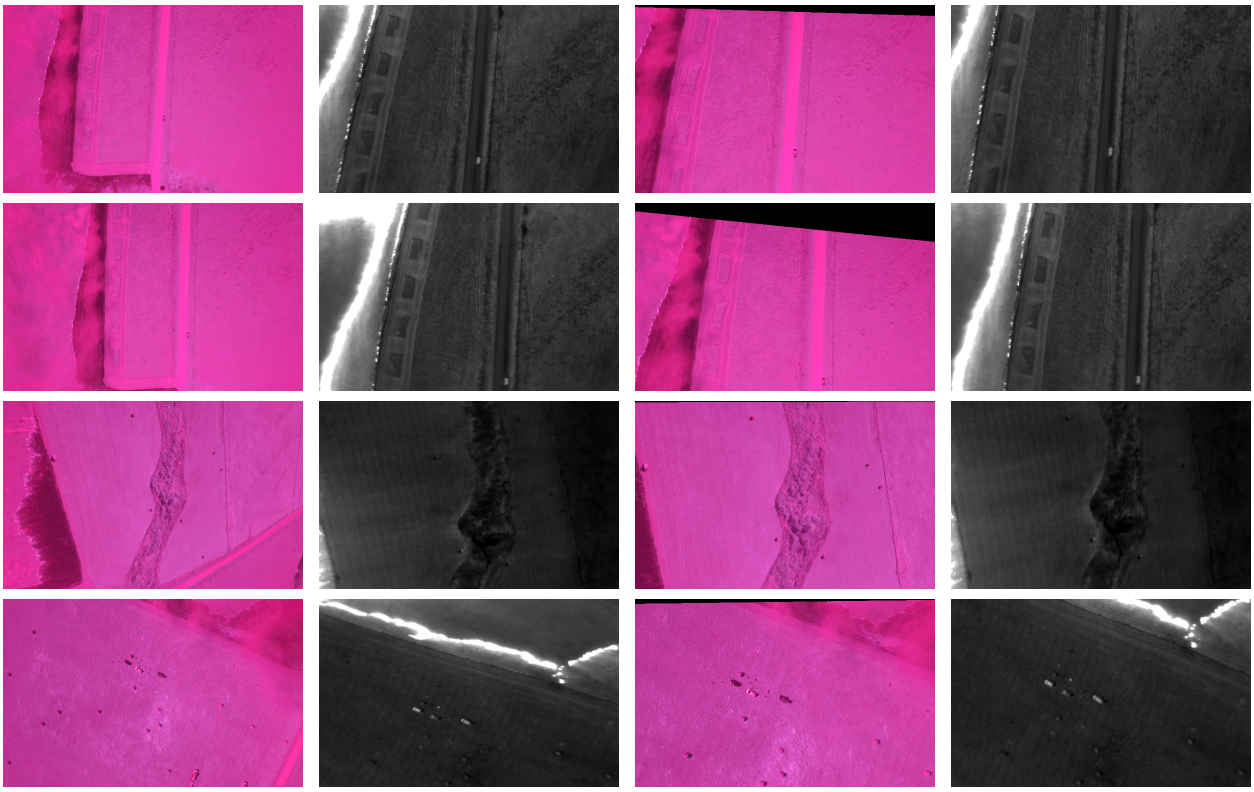

Figure A.1: First four GRAFFITI images: raw RGNIR (left column), histogram adjusted thermal (middle-left column), cropped RGNIR (middle-right column) and cropped thermal images (right column)